Geophysical Journal International

Geophys. J. Int. (2012) **191,** 1343–1360 doi: 10.1111/j.1365-246X.2012.05685.x

Properties of inelastic yielding zones generated by in-plane dynamic ruptures—II. Detailed parameter-space study

Shiqing Xu,[1] Yehuda Ben-Zion[1] and Jean-Paul Ampuero[2]

[1]*Department of Earth Sciences, University of Southern California, Los Angeles, CA* 90089*, USA. E-mail: shiqingx@usc.edu*
[2]*Seismological Laboratory, California Institute of Technology, Pasadena, CA, USA*

Accepted 2012 September 19. Received 2012 July 4; in original form 2012 February 8

SUMMARY

We perform a detailed parameter-space study on properties of yielding zones generated by 2-D in-plane dynamic ruptures on a planar fault with different friction laws and parameters, different initial stress conditions, different rock cohesion values, and different contrasts of elasticity and mass density across the fault. The focus is on cases corresponding to large strike-slip faults having high angle ($\Psi = 45^\circ$) to the maximum compressive background stress. The simulations and analytical scaling results show that for crack-like ruptures (1) the maximum yielding zone thickness $T_{\max}$ linearly increases with rupture distance L and the ratio $T_{\max}/L$ is inversely proportional to $(1 + S)^2$ with S being the relative strength parameter; (2) the potency density ε_0^p decays logarithmically with fault normal distance at a rate depending on the stress state and S; (3) increasing rock cohesion reduces $T_{\max}/L$, resulting in faster rupture speed and higher inclination angle Φ of expected microfractures on the extensional side of the fault. For slip pulses in quasi-steady state, T is approximately constant along strike with local values correlating with the maximum slip velocity (or final slip) at a location. For a bimaterial interface with $\Psi = 45^\circ$, the energy dissipation to yielding contributes to developing macroscopically asymmetric rupture (at the scale of rupture length) with the same preferred propagation direction predicted for purely elastic cases with Coulomb friction. When $\Psi = 10^\circ$, representative for thrust faulting, the energy dissipation to yielding leads to opposite preferred rupture propagation. In all cases, Φ is higher on average on the compliant side. For both crack and pulse ruptures with $\Psi = 45^\circ$, T decreases and ε_0^p increases for conditions representing greater depth. Significant damage asymmetry of the type observed across several large strike-slip faults likely implies persistent macroscopic rupture asymmetry (unilateral cracks, unilateral pulses or asymmetric bilateral pulses). The results on various features of yielding zones expected from this and other studies are summarized in a table along with observations from the field and laboratory experiments.

Key words: Microstructures; Elasticity and anelasticity; Rheology and friction of fault zones; Dynamics and mechanics of faulting; Fractures and faults; Mechanics, theory, and modelling.

1 INTRODUCTION

The internal structure of fault zones reflects processes and conditions that have operated during the fault history, and can affect various aspects of earthquakes and seismic radiation in the future. It is therefore important to understand the relations between properties of yielding zones around faults and different types of fault motion (e.g. crack/pulse ruptures and aseismic failure on planar and rough surfaces). The goal of this work is to contribute towards such understanding with a systematic investigation of characteristics of yielding zones generated by dynamic ruptures on a planar frictional interface. Xu *et al.* (2012), referred to hereafter as Paper I, described the computational method and defined several measures that can be used to quantify properties of yielding zones using example results. In this companion paper we perform a detailed parameter-space study on various features of off-fault yielding generated by different types of dynamic ruptures associated with different friction laws and parameters, different initial conditions, and different elastic and cohesion parameters of the surrounding media.

The example results in Paper I and previous studies (e.g. Ben-Zion & Shi 2005; Templeton & Rice 2008) demonstrated that the rupture style (crack versus pulse) and angle Ψ of the background maximum compressive stress relative to the fault influence strongly the distribution of off-fault yielding zones. In Section 2 of this paper we investigate the roles of other parameters (relative strength parameter S, rock cohesion, contrast of elasticity), and combinations of parameters corresponding to certain physical situations, in controlling rupture dynamics and properties of yielding zones including

© 2012 The Authors
Geophysical Journal International © 2012 RAS

their location, extent, intensity, symmetry properties, microfracture orientations and decay with fault-normal distance. The obtained results are used to develop correlations and scaling relations among different manifestations of yielding zones. In Section 3 the findings are discussed in relation to other models (e.g. fault motion on a rough surface) and observations from the field and the laboratory. The results provide improved criteria for interpreting various features of yielding zones around large strike-slip faults in terms of properties and conditions of earthquake ruptures on the faults.

2 DETAILED PARAMETER-SPACE STUDY

Fig. 1(a) presents the geometry and several basic ingredients of the employed model. Fig. 1(b) illustrates aspects of a model with fault roughness that will be discussed in comparison with the obtained results. Since pulse-like ruptures are more sensitive than crack-like ruptures to small changes of nucleation procedure, initial stress state, fault frictional properties and other ingredients (e.g. Zheng & Rice 1998; Ampuero & Ben-Zion 2008; Shi *et al.* 2008; Dunham *et al.* 2011a), we mainly use crack ruptures to clarify the basic effects of various parameters. Results from both rupture styles will be presented only when additional distinct features are seen for rupture pulses. We are primarily interested in yielding zones associated with large strike-slip faults, so the angle Ψ will be generally fixed at 45° unless mentioned otherwise. For convenience, Table 1 summarizes key equations from Paper I that are used frequently in this work. The parameters specifying material properties, friction laws, nucleation procedure and viscoplasticity have same values as in Paper I (table 1), except in cases of bimaterial ruptures where the elastic moduli and mass density of medium 2 are reduced. As in Paper I, we provide normalized values of physical quantities.

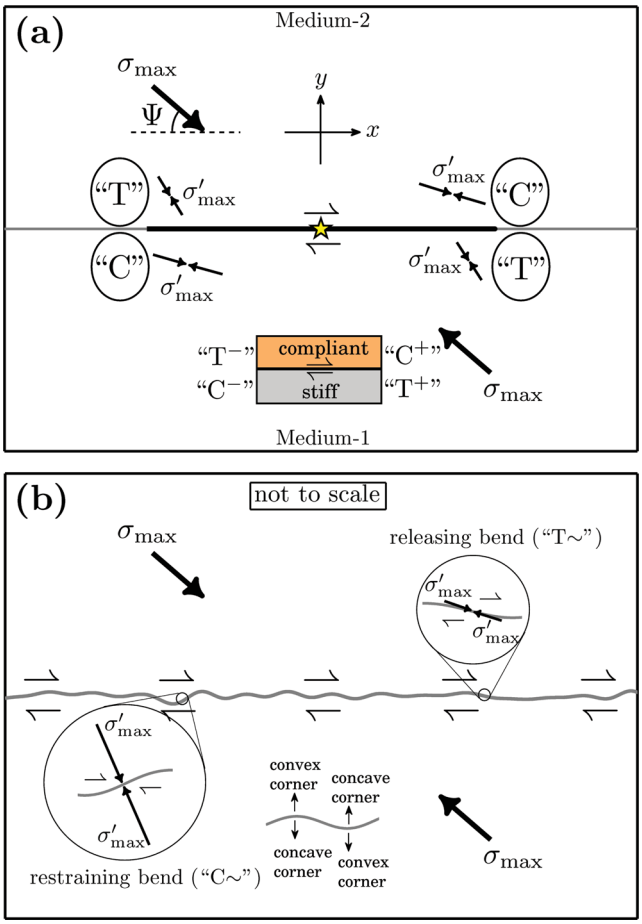

Figure 1. (a) Schematic diagram showing the migration of rupture tips along a planar fault, modified from Scholz *et al.* (1993). 'C' and 'T' represent the compressional and extensional quadrant(s), respectively. In the presence of a material contrast across the fault, the slip direction on the compliant side is referred to as the positive direction, and the quadrants in the same or opposite directions are distinguished by '+/−' signs. (b) Schematic diagram of a rough fault with geometric complexities, modified from Saucier *et al.* (1992) and Chester & Fletcher (1997). For both (a) and (b), the big arrows indicate the orientation of the far field background maximum compressive stress σ_{max}, while the small thin arrows represent the orientation and relative magnitude (indicated by the length) of the near-fault (dynamically or quasi-statically) perturbed maximum compressive stress σ'_{max}.

Table 1. Key equations.

$$S = \frac{\tau_s - \tau_0}{\tau_0 - \tau_d} \tag{T1}$$

$$\sigma^0_{xy} = \frac{f_s + S f_d}{1+S}(-\sigma^0_{yy}) \tag{T2}$$

$$\sigma^0_{xx} = \left[1 - \frac{2\sigma^0_{xy}}{\tan(2\Psi)\sigma^0_{yy}}\right]\sigma^0_{yy} \tag{T3}$$

$$\Psi = \frac{1}{2}\arccos\left[\frac{\sigma_{yy}-\sigma_{xx}}{\sqrt{(\sigma_{yy}-\sigma_{xx})^2+4\sigma^2_{xy}}}\right]\mathrm{sgn}(\sigma_{xy}) \tag{T4}$$

$$\Phi = \frac{1}{2}\arccos\left[\frac{-\varepsilon^p_{xx}}{\sqrt{(\varepsilon^p_{xx})^2+(\varepsilon^p_{xy})^2}}\right]\mathrm{sgn}(\varepsilon^p_{xy}) \tag{T5}$$

τ_s and τ_d: static and dynamic shear strength of the fault; τ_0: initial shear stress.
f_s and f_d: static and dynamic friction coefficient ($f_s = 0.6$, $f_d = 0.1$).
Ψ: angle of the maximum compressive stress relative to the fault (based on the stress tensor σ_{ij}), specified as the angle for the background stress if using σ^0_{ij}.
Φ: angle of the expected microfracture (aligned parallel to mode-I type) relative to the fault (based on the plastic strain tensor ε^p_{ij}).

2.1 Influence of the *S* parameter

The relative strength parameter S, defined as the ratio between strength excess and dynamic stress drop (eq. T1), is a key quantity connecting the background initial stress with fault frictional properties (Andrews 1976; Das & Aki 1977). In natural fault settings the S parameter may vary with the ratio of differential stress to the confining pressure, the values of the static and dynamic friction coefficients, and changing strike of fault segments in an approximately uniform regional stress field (e.g. Lockner & Beeler 2002; Oglesby *et al.* 2008; Shi *et al.* 2008). As in Paper I, we consider the range of values $S > 1.77$ known to generate ruptures with subshear speed, which is typical for most earthquakes. For the following investigation, the rock cohesion is set at $c = 0$.

To carefully investigate how the S parameter can influence the yielding zone properties, we choose the size of the applied nucleation zone L_{nucl} somewhat larger than the critical value L_c leading to dynamic instability (Palmer & Rice 1973):

$$L_c = \frac{16}{3\pi}\frac{\mu G_c}{(\tau_0 - \tau_d)^2}, \tag{1a}$$

where μ is the shear modulus, G_c is the fracture energy, and Poisson's ratio is assumed to be 0.25. We then fix the ratio of the applied

nucleation size $L_{\rm nucl}$ to the critical size L_c, so that comparable amount of energy is released in rupture nucleation for cases with different S values. The fracture energy evaluated from the evolution of stress as a function of slip during the breakdown process for slip-weakening friction (SWF) is $G_c = (1/2)|\sigma_n|(f_s - f_d)D_c$, where D_c is the slip-weakening distance. The critical size can be rewritten as

$$L_c = \frac{8}{3\pi}\frac{\mu D_c}{|\sigma_n|(f_s - f_d)}(1+S)^2. \tag{1b}$$

As the S value increases, the magnitude of the background normal stress has to increase to retain a comparable amount of released energy over the same nucleation length.

2.1.1 *Yielding zone extent and decay form*

Fig. 2 shows the distribution of plastic strain for crack-like rupture cases associated with different S values. As seen, the extent of the plastic yielding zone is relatively wide when the S value is relatively low but can be highly suppressed when S becomes high. This is consistent with results of Templeton & Rice (2008) for cases where off-fault plastic yielding primarily occurs on the same side (i.e. the extensional) of the fault. Templeton & Rice (2008) attributed this extent dependence on S partly to the closeness of initial stress state to yielding level (CF $= \tau^0_{\rm max}/\sigma^0_Y$) as a function of S. We provide

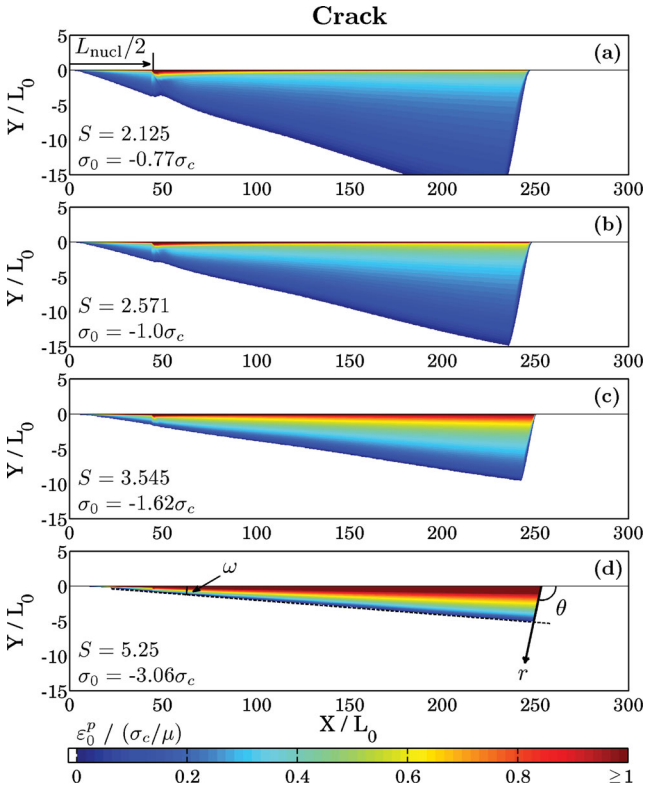

Figure 2. Plastic strain distribution for crack-like ruptures with $\Psi = 45^\circ$ and different values of S. The intensity of the plastic strain is quantified by the seismic potency density $\varepsilon_0^p = \sqrt{2\varepsilon_{ij}^p\varepsilon_{ij}^p}$ (see Paper I). The background normal stress σ_0 differs to preserve comparable energy release from the nucleation zone. In (d), r and θ are polar coordinates with origin at the moving rupture tip, and ω is a conventional angle quantifying the incremental rate of yielding zone thickness with the along-strike distance from the hypocentre (i.e. $\tan(\omega) \approx \Delta T/\Delta X$).

a quantitative explanation of the effect of S on the extent of the off-fault yielding zone in Section 2.1.2.

Next we use the procedure described in Paper I to investigate the off-fault decay of the potency density ε_0^p. We examine the variation of ε_0^p in the fault normal direction and define the thickness T of the yielding zone as the distance from the fault where ε_0^p decreases to zero. In Fig. 3 the sampling locations along the fault strike are mapped into different colours (see inset in Fig. 3a): each colour represents a trace normal to the fault strike, on the extensional side, starting from $X = 100L_0$ (blue) and ending at $X = 220L_0$ (red). The choice of the starting and ending points ensures that the selected range is neither within the nucleation zone nor too close to the rupture tip.

As shown in Figs 3(b)–(d), there are three distance ranges where the off-fault variation of ε_0^p follows distinct patterns. In region (1) the yielding zone is affected strongly by the artificial nucleation procedure (see inset in Fig. 3b) and is therefore excluded from detailed analysis. Once the rupture propagates away from that region ε_0^p may occur on both sides of the fault, but the summed value from both sides asymptotically approaches at zero distance a constant related to the breakdown process (inset in Fig. 3b). This feature is observed in all examined cases (a)–(d).

In the region labelled (2) in Fig. 3(c), representing most of the off-fault distance range where ε_0^p remains non-zero, there is a linear relation between ε_0^p and $\log(d_\perp)$ over the examined (one order of magnitude) range of $d_\perp$. This logarithmic decay is observed in all presented cases (Figs 3a–d), consistent with the results of Paper I and Yamashita (2000). The slope of the logarithmic decay for each case does not depend on the sampling location (reflected by the subparallel colour stripes), but it clearly varies for different rupture cases. The latter variation can be explained by the variable stress state which mainly determines the maximum value of ε_0^p close to the fault (the intercept with the vertical axis), and by the S parameter which controls the thickness of the yielding zone (the intercept with the horizontal axis).

As $d_\perp$ continues to increase beyond some point, ε_0^p rapidly tapers to zero in a final third regime. We find a linear relation between the thickness of the yielding zone and the along-strike distance from the hypocentre (inset in Fig. 3d). This feature is consistent with the large-scale view in Fig. 2 (which is usually difficult to obtain in the field) that the off-fault yielding zones for the simulated crack cases have a triangular shape.

2.1.2 *Theoretical scaling relation*

How far the activated off-fault yielding zone can extend depends on the interaction between the background stress field σ_{ij}^0 and the slip-induced incremental stress field $\Delta\sigma_{ij}$ at some transitional distance range from the rupture tip where the total stress just reaches the off-fault yielding strength. Following Ben-Zion & Ampuero (2009), we develop a scaling relation between yielding zone thickness and the S parameter with order of magnitude quantities. For simplicity, we adopt here a singular crack model rather than a model with a finite cohesive zone. Differences between the two models are mentioned when necessary. Based on the singular crack model (e.g. Freund 1990), the incremental stress field $\Delta\sigma_{ij}$ in the vicinity of the crack tip can be described as:

$$\Delta\sigma_{ij} = \frac{K_{\rm II}^d}{\sqrt{2\pi r}}\Sigma_{ij}(\theta, v_r) + \begin{bmatrix} 0 & -\Delta\tau \\ -\Delta\tau & 0 \end{bmatrix} + O(\sqrt{r}), \tag{2}$$

where r and θ are polar coordinates with the origin at the crack tip (Fig. 2d), $\Delta\tau = \tau_0 - \tau_d$ is the stress drop, $K_{\rm II}^d = k_{\rm II}(v_r)\Delta\tau\sqrt{\pi L}$

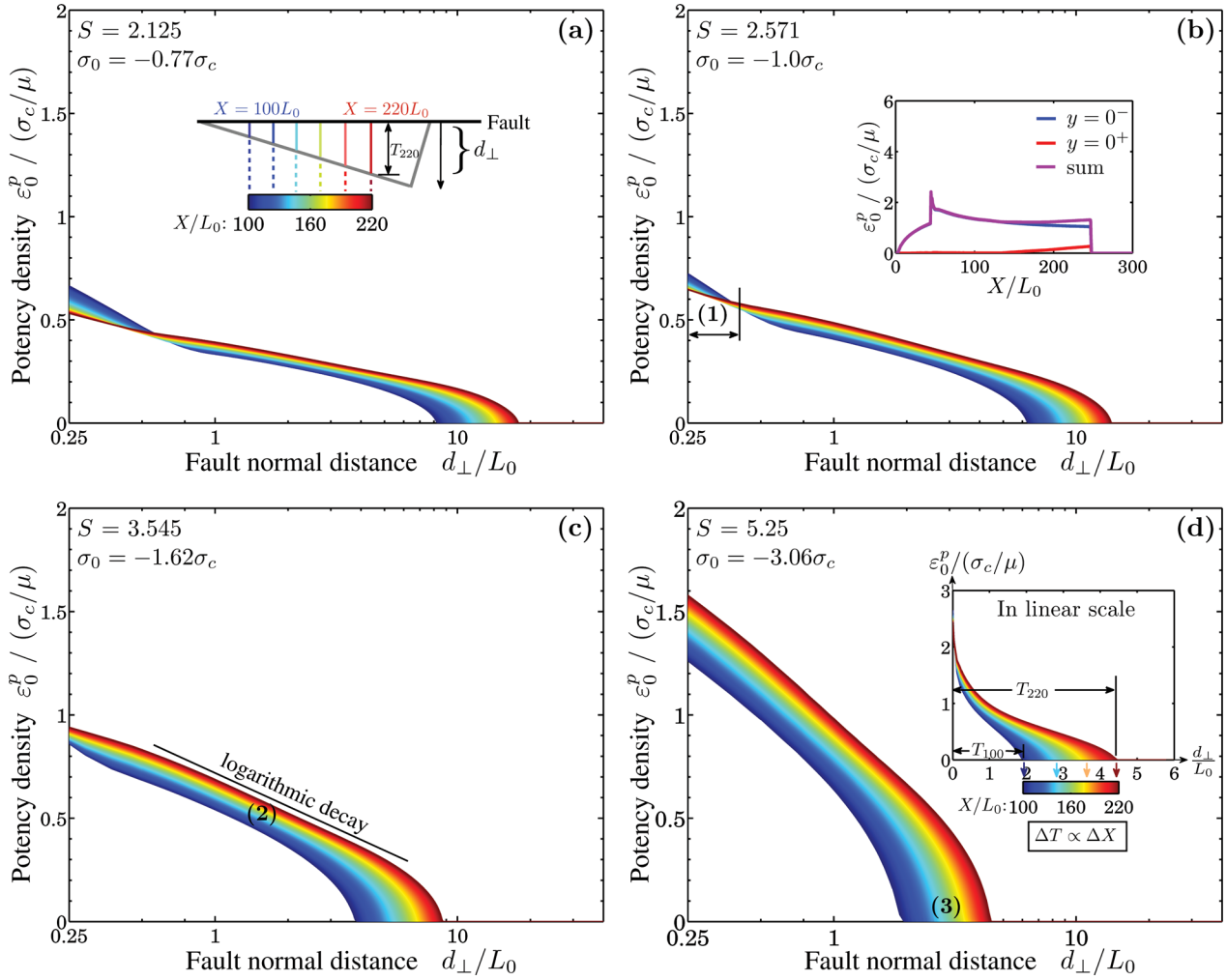

Figure 3. Off-fault decay of the seismic potency density ε_0^p versus fault normal distance $d_\perp$ for crack-like ruptures associated with different S and σ_0 values. The schematic diagram in (a) illustrates the employed mapping between sets of colours and distance from hypocentre. The inset in (b) shows the variation of ε_0^p from each side of the fault (or the summed value) along the strike. The inset plot in (d) reproduces the result in a double-linear scale.

is the dynamic stress intensity factor with $k_{\rm II}(v_r)$ being a universal function of rupture speed v_r and L denoting the half length of the crack (e.g. Broberg 1999).

At the farthest distance $r_{\max}$ from the rupture tip where off-fault yielding can be activated, the total stress field $\sigma_{ij} = \sigma_{ij}^0 + \Delta\sigma_{ij}$ is expected to just satisfy the yielding criterion for cohesionless rocks (Xu *et al.* 2012):

$$\sqrt{\sigma_{xy}^2 + (\sigma_{xx} - \sigma_{yy})^2/4} = -0.5(\sigma_{xx} + \sigma_{yy})\sin(\phi), \tag{3}$$

where ϕ is the internal friction angle. Writing σ_{ij}^0 and $\Delta\tau$ (normalized by σ_0) as functions of S and fault friction coefficients for $\Psi = 45^\circ$, using eq. (2) to express $\Delta\sigma_{ij}$ as functions of $k_{\rm II}(v_r)$, $\Delta\tau$, $\sqrt{L/r_{\max}}$ and $\Sigma_{ij}(\theta, v_r)$, and using the obtained expression for σ_{ij} in eq. (3), we have

$$\frac{r_{\max}}{L} = \eta \frac{k_{\rm II}^2(v_r)\cdot A^2}{(1+S)^2}, \tag{4}$$

where η is a factor of order 1 (to be determined numerically) and A is a dimensionless quantity depending on $\Sigma_{ij}(\theta, v_r)$, friction coefficients and ϕ. Projecting $r_{\max}$ on the fault normal direction to estimate the maximum yielding zone thickness $T_{\max}$, we get

$$\frac{T_{\max}}{L} = \eta \frac{k_{\rm II}^2(v_r)\cdot A^2\cdot|\sin(\theta)|}{(1+S)^2}. \tag{5}$$

For any v_r, we can search for a value of θ that maximizes $T_{\max}/L$ in eq. (5). Assuming $v_r = 0.827c_s$ typical for our cases, we get $\theta \approx -130^\circ$. This is consistent with the simulation results (see the yielding pattern near the rupture tips in Fig. 2, noting the vertical exaggeration of factor 3.75). Fig. 4 shows a comparison between the numerical simulation results and eq. (5) with $v_r = 0.827c_s$ and $\theta \approx -130^\circ$. For simplicity, we also adopt $k_{\rm II}(v_r = 0.827c_s) \approx 0.375$ (Broberg 1999, fig. 6.9.8). The prediction with $\eta = 1$ (corresponding exactly to the truncated theoretical solution of eq. 2) underestimates the ratio $T_{\max}/L$ (dashed line in Fig. 4). This may be explained by the fact that the abrupt drop of shear stress in the singular solution (given by the second term of eq. 2) leads to lower average shear stress behind the rupture tip (where major plastic yielding occurs in Fig. 2) compared with the non-singular model associated with a gradual shear stress drop over a finite length scale. Using a correction factor $\eta = 1.72$ provides a good agreement between the singular crack model with prescribed rupture process and the non-singular numerical results associated with spontaneous rupture and SWF.

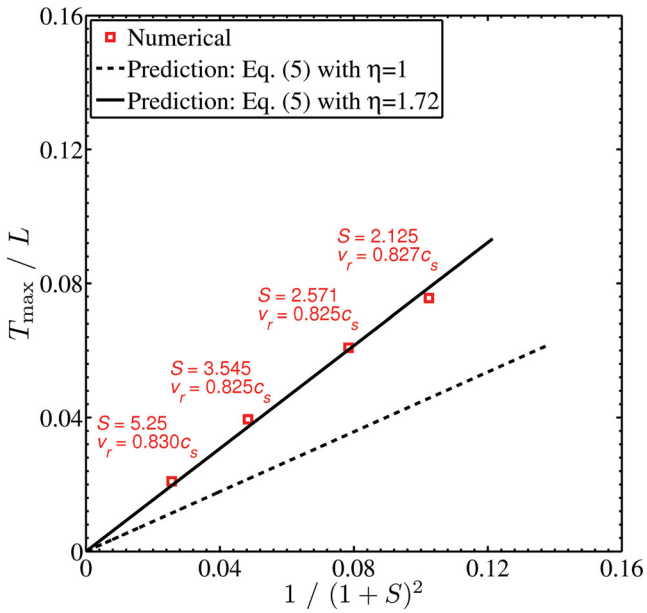

Figure 4. Comparison of the numerical results and theoretical prediction of eq. (5) (with assumed $\theta = -130^\circ$ and $v_r = 0.827c_s$) on the scaling relation between $T_{\max}/L$ and S. Numerical results are obtained by first calculating $\Delta T/\Delta X$ based on the measurements in Fig. 3, and then converting it into angle ω to calculate $T_{\max}/L$ through the relation $T_{\max}/L = \sin(\omega)\sin(|\theta|)/\sin(|\theta| - \omega)$ (see angle definition in Fig. 2d).

A more detailed analysis may employ simulations with additional low values of S (before leading to supershear ruptures) or very high S values. At the former limit, additional terms of eq. (2) (i.e. those included in $O(\sqrt{r})$) may have to be considered, because when $T_{\max}/L$ is expected to be fairly high the above analyzed terms may not be sufficient to dominate the contribution to $\Delta\sigma_{ij}$. At the latter limit when $T_{\max}/L$ is expected to be very low, eq. (5) will reduce to

$$\frac{T_{\max}}{L} \propto \frac{1}{S^2}. \tag{6}$$

In this limit the finite size of the rupture tip cohesive zone, which is ignored in eq. (2), should become important. In addition, this limit may approximate the case examined by Poliakov *et al.* (2002) for semi-infinite cracks ($L \to \infty$) with almost zero stress drop ($S \to \infty$).

We note that the scaling relations given by eqs (5) and (6) do not apparently depend on the absolute value of the stress field or any length scale, but rather imply a dependence of one non-dimensional quantity on another. These scaling implications, along with the previously reported self-similar slip profiles in Paper I, can help identify crack-like earthquake ruptures based on field data, and may be useful for jointly constraining (or inferring) the remote stress field and/or fault frictional properties. As noted by Ben-Zion & Ampuero (2009), theoretical estimates of $T_{\max}/W$ for pulses of width W can be derived in analogous fashion, with an appropriate function $f_{\rm II}(v_r, v_h)$ dependent also on the speed of the healing front v_h.

2.2 Influence of rock cohesion

Several studies showed that the assumed value of rock cohesion can influence rupture dynamics and off-fault yielding (e.g. Ben-Zion & Shi 2005; Duan 2008; Ma & Andrews 2010). The effective value of this quantity usually varies with rock type and confining pressure, and depends strongly on the initial rock damage (e.g. Scholz 2002; Jaeger *et al.* 2007). Rock cohesion generally has two major effects that can influence the measurable properties associated with off-fault yielding. The first is directly related to the extent of the yielding zone. As illustrated in Table 2, with the same initial stress state and nucleation procedure, increasing rock cohesion can reduce the size of the yielding zone and decrease, for crack ruptures, the ratio of yielding zone thickness to rupture distance. This direct effect is naturally expected from the adopted yielding criterion and is generally consistent with the appearance of c in the closeness to failure parameter of Templeton & Rice (2008):

$$\mathrm{CF} = \frac{\sqrt{(\sigma^0_{xx} - \sigma^0_{yy})^2/4 + (\sigma^0_{xy})^2}}{-(1/2)(\sigma^0_{xx} + \sigma^0_{yy})\sin\phi + c\cos\phi}. \tag{7}$$

Table 2. Relation between the incremental rate of yielding zone thickness with along-strike distance from the hypocentre and rock cohesion c.

	$c = 0.0\sigma_c$	$c = 0.2\sigma_c$	$c = 0.4\sigma_c$	$c = 0.6\sigma_c$
$\Delta T/\Delta X$	0.0635	0.0364	0.0221	0.0139

The second effect of rock cohesion is related to the microfracture orientation close to the fault. This effect operates through the evolving rupture speed that is correlated with the amount of off-fault yielding as a function of rock cohesion. To investigate the effect of rock cohesion on off-fault dynamic stresses, and hence yielding, we measure the expected microfracture orientation at a distance of $0.125L_0$ (half spectral element) from the fault plane on the extensional side for $\Psi = 45^\circ$ and smooth the measurements over an along-strike length of $0.25L_0$ (one spectral element).

Fig. 5(a) shows the predicted results for three friction coefficient ratios of SWF (with f_s fixed at 0.6), based on the non-singular crack model of Poliakov *et al.* (2002). For all three cases, the angle Φ of the expected microfractures relative to the fault (aligned to mode I type) monotonically increases with the normalized rupture speed v_r/c_s and asymptotically approaches 90° near the limit level c_R/c_s. Fig. 5(b) shows the variation of the normalized rupture speed v_r/c_s (solid curves with scale at the left vertical axis) and the inferred angle Φ (discrete markers with scale at the right vertical axis) obtained in the numerical simulations for three c values. For a given rock cohesion the variations of Φ are positively correlated with those of v_r/c_s. When comparing different cases with the same rupture propagation distance, the angle Φ increases with the rupture speed (associated with increasing rock cohesion).

The inset plot in Fig. 5(b) explicitly illustrates the correlation of Φ with v_r/c_s in the range indicated by the dashed box. The numerical results are generally in good agreement with the analytic prediction for $f_d/f_s = 0.167$ (which corresponds to $f_d = 0.1$ and $f_s = 0.6$). The systematic deviation of the numerically inferred angle Φ from the analytic prediction may be explained by the essential differences between the numerical and analytic models, e.g. with or without stress relaxation once reaching the yielding criterion. We note that as c becomes higher, reducing the influence of stress relaxation, the numerical results get closer to the analytic prediction.

2.3 Influence of material contrast across the fault

So far the properties of dynamic ruptures and off-fault yielding zones have been investigated in an isotropic homogeneous medium. However, large natural faults tend to separate different rock bodies

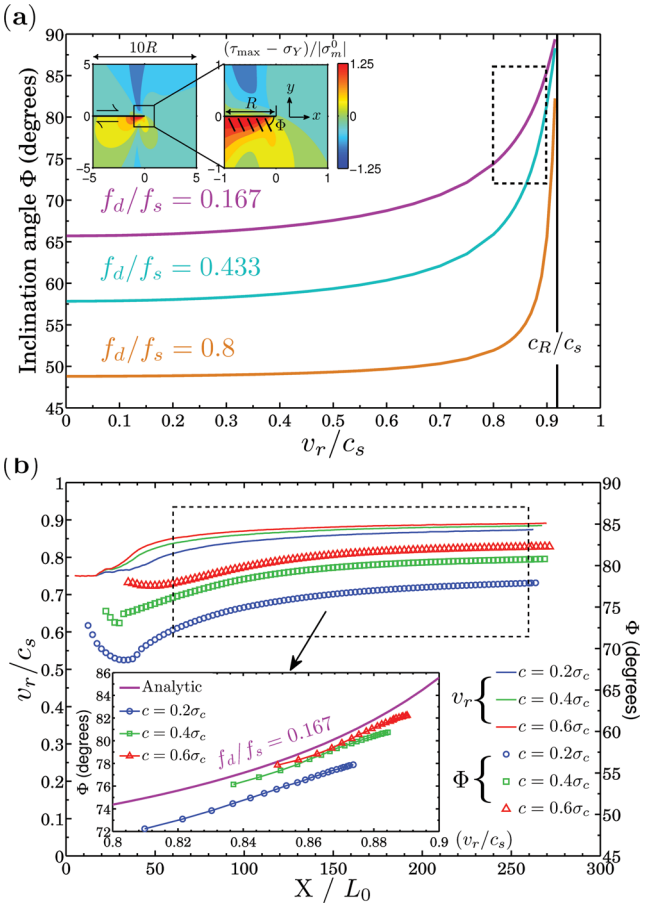

Figure 5. (a) Analytic prediction of close-to-fault microfracture orientation as a function of rupture speed v_r with a fixed static friction coefficient $f_s = 0.6$, based on the non-singular crack model of Poliakov *et al.* (2002) ($-R < x - v_r t < 0$, $y \approx 0^-$, with R being the size of process zone). (b) Variation of numerically inferred close-to-fault microfracture orientation and rupture speed along strike for cases with different rock cohesion values. The inset shows the comparison between the numerical results in the dashed box and the analytic prediction in about the same selected range.

(e.g. Ben-Zion 1990; Le Pichon *et al.* 2005; McGuire & Ben-Zion 2005; Thurber *et al.* 2006). In this section, we incorporate elasticity contrast across the fault into our numerical procedure (Ampuero & Ben-Zion 2008) and investigate how the bimaterial effect can influence the generation and distribution of off-fault yielding.

As in Ben-Zion & Shi (2005) and later studies, we find that the locations of the off-fault yielding can be strongly affected by the existence of a bimaterial interface. In an isotropic homogeneous medium, although the off-fault yielding zone is usually asymmetrically distributed across the fault (for a single event), the partition pattern with respect to the hypocentre is symmetric. The latter symmetry can be broken by the presence of a material contrast across the fault. This and the different stress concentrations between crack and pulse type ruptures lead to various changes in yielding zones properties.

Fig. 6 shows the distribution of plastic strain with 20 per cent material contrast (see Paper I for definition) for crack-like ruptures generated using SWF. When $\Psi = 10^\circ$, typical for thrust faults, plastic strain is dominantly distributed on the compliant side in the positive direction, while it apparently extends to both sides of the fault in the negative direction, showing an asymmetric pattern with respect to the hypocentre. When $\Psi = 45^\circ$, typical for

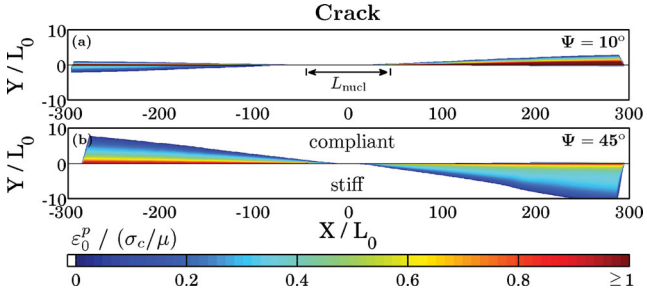

Figure 6. Plastic strain distribution for crack-like ruptures on a bimaterial interface with 20 per cent contrast for (a) $\Psi = 10^\circ$ and (b) $\Psi = 45^\circ$. For both cases, $\sigma_{xy}^0 = 0.24\sigma_c$, $\sigma_{yy}^0 = -1.0\sigma_c$ and $c = 0.2\sigma_c$.

strike-slip faults, plastic strain is mainly distributed with the employed parameters in the two extensional quadrants, generally following the pattern in an isotropic homogeneous medium. However, the off-fault extent of the yielding zone is wider on the stiff side (in the positive direction) than on the compliant side (in the negative direction), consistent with the numerical results of Duan (2008).

Fig. 7 shows the slip velocity profiles at different times and the estimated rupture speed beyond the nucleation zone for the crack cases of Fig. 6. The results confirm that the rupture propagates as asymmetric bilateral crack for both cases, consistent with the expectation that slip-weakening friction with relatively large

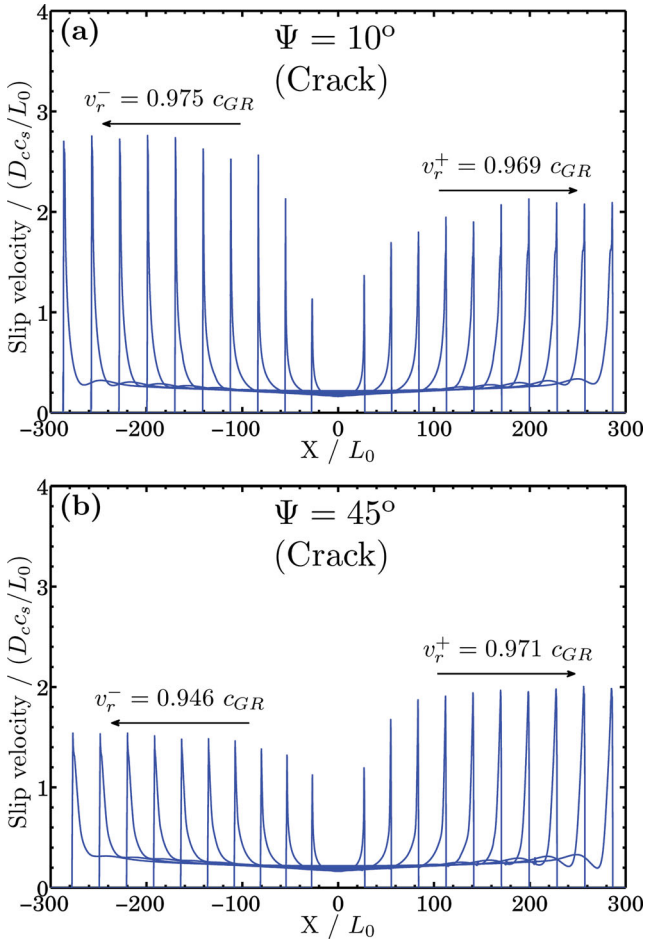

Figure 7. Slip velocity profiles for the crack cases of Fig. 6 with the generalized Rayleigh wave speed being $c_{GR} = 0.825 c_s^{fast}$ for $\gamma = 20$ per cent.

$f_s - f_d$ and smooth nucleation procedures lead to asymmetric bilateral cracks on a bimaterial interface (e.g. Harris & Day 1997; Shi & Ben-Zion 2006; Rubin & Ampuero 2007). In such cases, the direction with higher propagation speed and peak slip velocity depends, along with the generation of off-fault yielding, strongly on Ψ. When $\Psi = 10^\circ$, the left propagating tip has faster rupture speed and higher peak slip velocity than the one propagating to the right (Fig. 7a), in contrast to the prediction for a purely elastic model in the subshear regime (e.g. DeDontney *et al.* 2011). As Ψ increases to 45°, the tip propagating to the right has (Fig. 7b) faster speed and higher peak slip velocity, consistent with the prediction for a purely elastic model (e.g. Shi & Ben-Zion 2006; Brietzke *et al.* 2009).

The above differences in rupture and slip velocities may be explained by the generation of off-fault yielding, whose distribution depends strongly on Ψ and on the material contrast. When $\Psi = 10^\circ$, more plastic strain is distributed (Fig. 6a) on the compliant side (in the positive direction) than on the stiff side (in the negative direction). Therefore, although the right propagating rupture may be encouraged by the tensile change of normal stress right behind the rupture front, the energy absorbed by the larger off-fault yielding leads to lower rupture and peak slip velocities. When $\Psi = 45^\circ$, the left propagating rupture generates larger plastic strain (Fig. 6b) and compressive dynamic change of normal stress. Both effects lead to higher rupture and slip velocities in the right (positive) direction. These features are generally consistent with the numerical results of DeDontney *et al.* (2011) with off-fault elasto-plastic response. We note that DeDontney *et al.* (2011) reported failed ruptures under $\Psi = 45^\circ$ and unilateral ruptures in the positive direction under $\Psi = 35^\circ$, in contrast to our asymmetric bilateral crack under $\Psi = 45^\circ$. These small differences may be due to details associated with the employed material contrast, S parameter, and the nucleation procedure. It should be mentioned that the bimaterial interface in our study separates as in, e.g. Ben-Zion & Shi (2005) and DeDontney *et al.* (2011), materials of different elastic moduli and mass densities. The lower density on the compliant side contributes to generation of higher plastic strain on that side compared to the stiff side. This, in turn, leads to reversed preferred rupture direction under low Ψ values. Duan (2008) used same mass density across the fault in his studies of bimaterial ruptures and obtained higher magnitude of plastic strain on the stiff side in contrast to our results and to those of DeDontney *et al.* (2011).

In addition to the asymmetry of off-fault yielding zones with respect to the hypocentre, we wish to find more signatures that may help identify preferred rupture direction or reflect the existence of a bimaterial fault. Among all the quantities that have been investigated before, we find that off-fault microfracture orientation may be a good indicator. Fig. 8 shows the inferred results for the crack cases of Fig. 6. When $\Psi = 10^\circ$, the inferred angle Φ on the compliant side has a higher average value than the one on the stiff side over the same off-fault distance range (see 'C^+' versus 'C^-' and 'T^-' versus 'T^+' in Fig. 8a). Moreover, an interesting feature with a reversed sign of Φ is observed in 'C^-', probably reflecting the interaction between the slip-induced stress change and the local dynamic change of normal stress. When $\Psi = 45^\circ$, although the major plastic yielding switches to the extensional quadrants, the inferred angle Φ still has a higher average value on the compliant side ('T^-') than on the stiff side ('T^+'). The results hold for off-fault yielding produced by single asymmetric bilateral ruptures. The cumulative effect of multiple such ruptures with different hypocentre locations is expected to produce off-fault yielding on both sides of the fault, but still with a higher average angle Φ on the compliant side than on the stiff one.

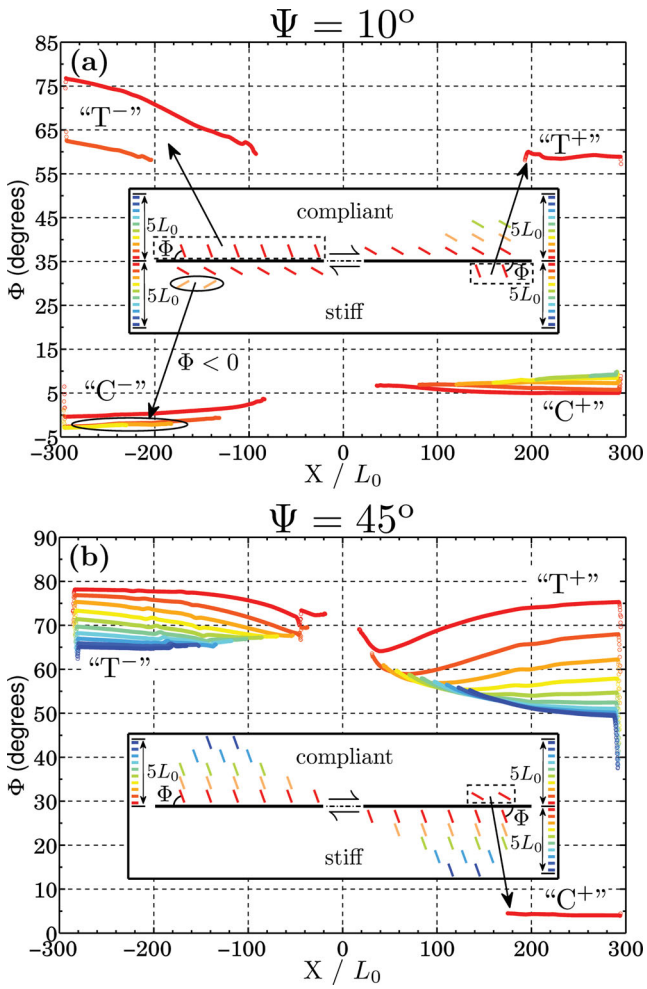

Figure 8. Inferred microfracture orientation for the crack cases of Fig. 6 (see Fig. 1a for quadrant notations).

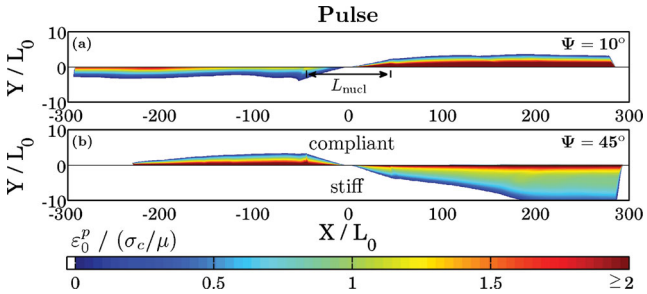

Figure 9. Plastic strain distribution for pulse-like ruptures on a bimaterial interface with 20 per cent contrast for (a) $\Psi = 10^\circ$ and (b) $\Psi = 45^\circ$. For both cases, $\sigma^0_{xy} = 1.04\sigma_c$, $\sigma^0_{yy} = -4.0\sigma_c$ and $c = 0$.

Next we briefly discuss results for pulse-like bimaterial ruptures, whose dynamic behaviour is more sensitive to the generation of off-fault yielding. When $\Psi = 10^\circ$, the rupture propagates as an asymmetric bilateral pulse with higher rupture and slip velocities to the left (Figs 9a and 10a). In contrast, as Ψ increases to 45°, the left propagating pulse is arrested after some distance and the rupture eventually becomes a unilateral pulse propagating to the right (Figs 9b and 10b). For both $\Psi = 10^\circ$ and $\Psi = 45^\circ$, the local T value correlates with the maximum slip velocity and final slip (not shown here) at the same location (Figs 9 and 10), consistent

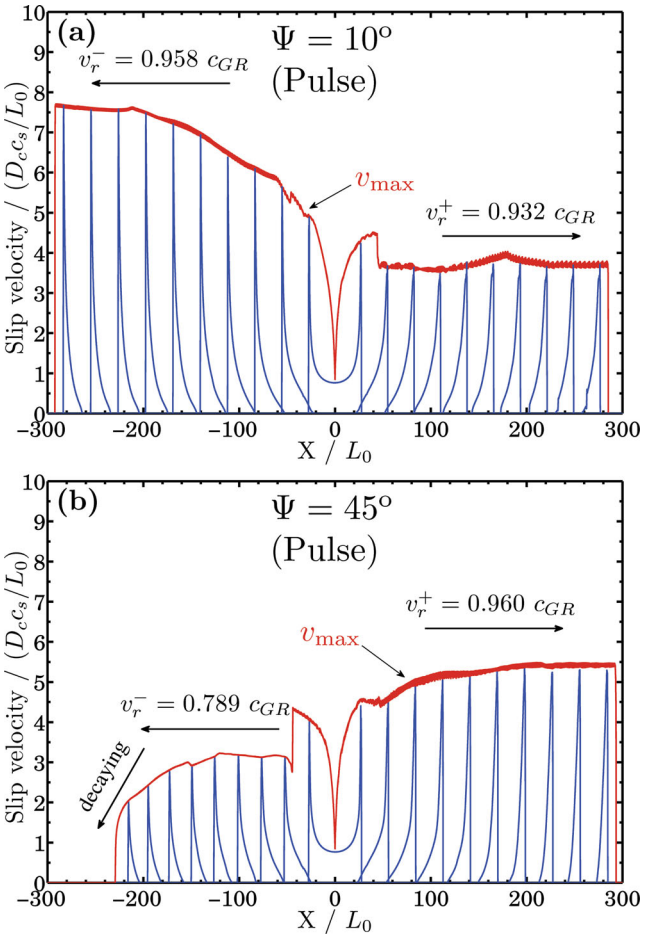

Figure 10. Slip velocity profiles for the pulse cases of Fig. 9 with the generalized Rayleigh wave speed being $c_{GR} = 0.825 c_s^{\text{fast}}$ for $\gamma = 20$ per cent.

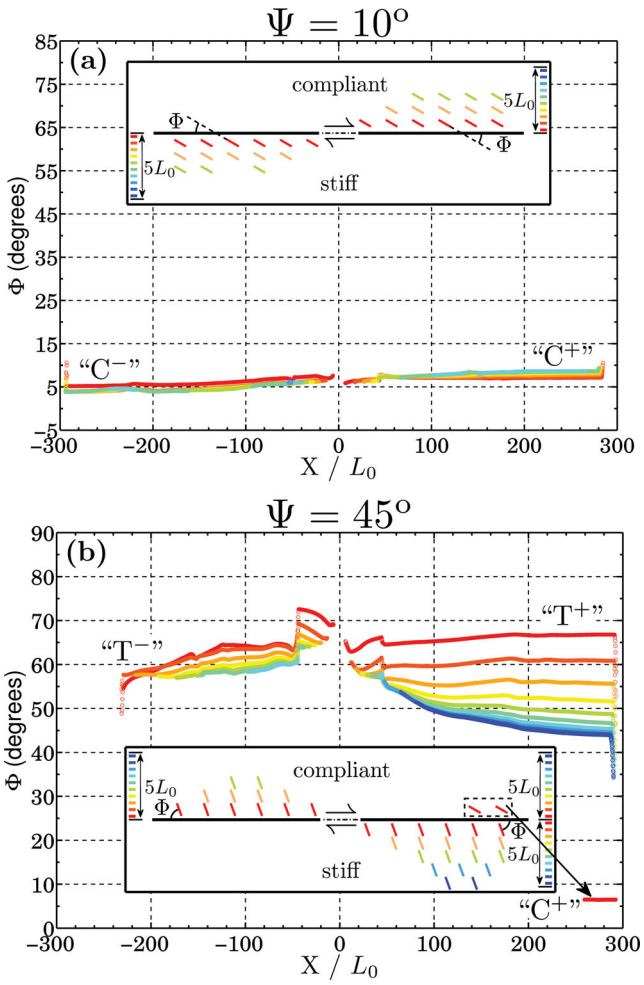

Figure 11. Inferred microfracture orientation for the pulse cases of Fig. 9.

with the earlier results of Ben-Zion & Shi (2005). The correlation with final slip can be related to the analysis in Section 2.1.2 and the previous work by Ben-Zion & Ampuero (2009) that both the final slip and the yielding zone thickness are expected to scale with the pulse width. The inferred angle Φ at a given propagation distance has higher average value on the compliant side than on the stiff side for both cases (Fig. 11).

The above dynamic features can again be explained by the interaction between the generation of off-fault yielding and the bimaterial effect through the angle Ψ. However, we emphasize that the dynamic behaviour of a propagating pulse is more sensitive to off-fault yielding than that of a crack. With the same bimaterial fault interface, the examined cracks continue to propagate bilaterally (asymmetrically) with and without off-fault yielding, while the studied pulses can switch from being asymmetrically bilateral to unilateral, depending on the amount of off-fault yielding. The latter may be adjusted by changing the value of rock cohesion and/or S parameter. This implies that with a material contrast across the fault, the asymmetry of the dynamic behaviour and the associated off-fault yielding zones for pulse type ruptures can be more prominent than that for cracks. In particular, the cumulative effect of the case shown in Fig. 9(b) (with many hypocentre locations) is expected to produce much more extensive off-fault yielding on the stiff side than on the compliant side, in agreement with the numerical results of Ben-Zion & Shi (2005) based on Coulomb type friction and various geological and seismological observations (e.g. Lewis *et al.* 2005, 2007; Dor *et al.* 2006, 2008; Mitchell *et al.* 2011).

2.4 Ruptures at different depth sections

So far we investigated properties of rupture-induced inelastic yielding zones by individually varying several controlling parameters including the background stress state (in Paper I), S parameter, rock cohesion and a possible contrast of rock elasticity and density across the fault. Here we explore how combinations of these parameters representing different depth sections can influence the generation and properties of the inelastic yielding zones, with and without material contrast across the fault. In particular, we define three typical depth sections, referred to as 'shallow', 'intermediate' and 'deep', considering that the on-fault initial shear and normal stresses increase with depth. We also assume that the value of rock cohesion increases with depth, in agreement with laboratory observations that damage healing and cohesion increase with σ_n (e.g. Johnson & Jia 2005; Jaeger *et al.* 2007).

2.4.1 Without material contrast across the fault

We first quantify the effect of depth on crack-like ruptures (see caption of Fig. 12). The angle Ψ is fixed at 45°, consistent with our focus on large strike-slip faults, and the shear to normal stress

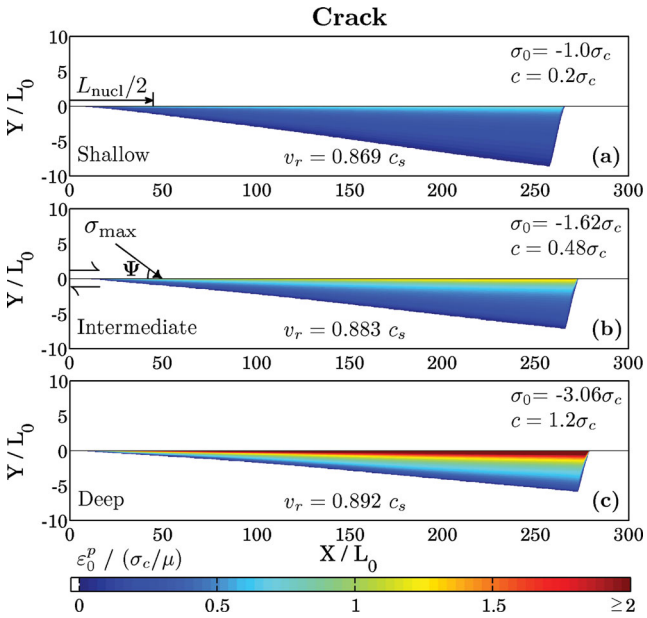

Figure 12. Plastic strain distribution for crack-like ruptures at conditions representing different depth sections without material contrast across the fault. For all cases, $\tau_0/(-\sigma_0) = 0.24$ or $S = 2.571$. Parameters for different depth sections are: (a) $\sigma_0 = -1.0\sigma_c$, $c = 0.2\sigma_c$; (b) $\sigma_0 = -1.62\sigma_c$, $c = 0.48\sigma_c$; (c) $\sigma_0 = -3.06\sigma_c$, $c = 1.2\sigma_c$.

ratio $\tau_0/(-\sigma_0)$ is fixed at 0.24, associated with $S = 2.571$. To allow comparable amount of released energy to nucleate the rupture, we also fix the ratio of the applied nucleation size $L_{\rm nucl}$ to the critical size L_c for different cases, leading to smaller $L_{\rm nucl}$ with increasing depth (σ_0).

Fig. 12 shows the plastic strain distribution for crack ruptures at the three depth sections. As expected, the off-fault yielding zone for all three cases displays a triangular shape that is mainly distributed in the extensional quadrant (only the right half is shown due to the symmetry). However, the off-fault extent and magnitude of the plastic strain vary with depth. The thickness of the yielding zone becomes progressively narrower for conditions representing greater depth due to the increasing rock cohesion. The magnitude of the plastic strain consistently increases with depth due to the increasing background stress and dynamic stress drop. These features are consistent overall with the early 2-D results of Ben-Zion & Shi (2005) and Rice *et al.* (2005), the more recent 2-D and 3-D simulation results of Ma (2008), Ma & Andrews (2010) and Kaneko & Fialko (2011), and geological and seismological observations of 'flower-like' fault zone structure with depth (e.g. Rockwell & Ben-Zion 2007, and references therein). In particular, seismic trapped waves and related studies imply that low velocity fault zone layers with considerable thickness are generally limited to the top several kilometres of the crust (e.g. Ben-Zion *et al.* 2003; Lewis *et al.* 2005; Lewis & Ben-Zion 2010; Yang & Zhu 2010; Yang *et al.* 2011).

We note that, as in Ben-Zion & Shi (2005) and later studies, we used a fairly low cohesion value for shallow depth and relatively high c for deeper sections. It appears that the assumed value of rock cohesion at different depth sections plays a more important role in controlling the yielding zone extent than other depth-dependent conditions such as the normal stress. This is anticipated by the scaling relation of eq. (5), indicating that when c is negligible, T is similar for depth ranges with similar S parameter and rupture length, similar angle θ near the rupture tip (Fig. 2d), and comparable rupture speeds. To verify this expectation we performed simulations with same rock cohesion for different depth sections and found no prominent variation of yielding zone thickness with depth, as long as the assumed c value remains a small fraction (possibly zero) of σ_n at the shallowest examined depth. This is consistent with the 3-D numerical simulation by Ma & Andrews (2010) of crack-like rupture with constant non-zero rock cohesion. As mentioned, laboratory data indicate that rock cohesion should generally increase with depth (e.g. Jaeger *et al.* 2007).

Fig. 13 shows the expected microfracture orientation over certain off-fault distance range for the crack cases of Fig. 12. The results generally display a similar pattern for all three depth sections: Φ has a maximum value approaching 80° at a fault normal distance $d_\perp \approx 0.4L_0$ and it gradually decreases to about 60° at $d_\perp \approx 5L_0$ (Figs 13a–c). This similarity may be explained by the fact that the dynamic stress drop is proportional to the background stress, and the total stress in eq. (T4) and plastic strain in eq. (T5) increase linearly with depth. Despite the overall similarity, the difference in the inclination angle Φ can still be observed by investigating close-to-fault microfractures ($d_\perp = 0.125L_0$) due to rupture speed variation with depth (Fig. 13d).

Fig. 14 shows the plastic strain distribution for pulse type ruptures for conditions representing two depth sections. Since the dynamic behaviour of rupture pulses is more sensitive to the generation of off-fault yielding (and many other factors), only two depth sections, referred to as 'shallow' and 'intermediate', are used. The assumed values for S and c are slightly different from those used for the crack ruptures but are self-consistent with variable depth conditions. In contrast to the crack cases of Fig. 12, the yielding zone thickness for the pulse cases only slightly decreases with depth and approaches a constant value along strike after its initial growth. The mild depth variation might be explained by the tendency of the ruptures generated with the employed rate-and-state friction law to evolve from steady-state to self-similar pulse behaviour with increasing dynamic stress drop while keeping all other constitutive parameters unchanged (e.g. Zheng & Rice 1998; Nielsen & Carlson 2000; Ampuero & Ben-Zion 2008). This is related to the fact that self-similar (growing) ruptures usually produce broader yielding zones than pulse-like ruptures that are approximately in steady-state (Ben-Zion & Shi 2005; Xu *et al.* 2012). The case representing 'intermediate' depth is associated with higher stress than the one representing 'shallow' section. As a result, the more energetic rupture pulse at greater depth may partially counter or even overcome the effect of the increased c with depth.

Fig. 15 shows the expected microfracture orientation for the pulse cases of Fig. 14. The inferred angle Φ has an average value around 70° at both depth sections, and is slightly higher at the intermediate depth probably due to the faster rupture speed at that depth (e.g. Rice *et al.* 2005). Another interesting phenomenon is that the angle Φ is approaching a constant as a function of fault normal distance (characterized by the colour) beyond $X = 200L_0$ at shallow depth (Fig. 15a). This and the constant yielding zone thickness beyond $X = 200L_0$ in Fig. 14(a) imply that the rupture pulse approaches quasi-steady propagation conditions around $X = 200L_0$.

2.4.2 *With material contrast*

Here various degrees of material contrast across the fault are added to represent different depth ranges. Following Ben-Zion & Shi (2005), the degree of material contrast γ decreases with depth: $\gamma = 20$ per cent for 'shallow', $\gamma = 10$ per cent for 'intermediate' and $\gamma = 5$ per cent for 'deep' sections (see Paper I for definition).

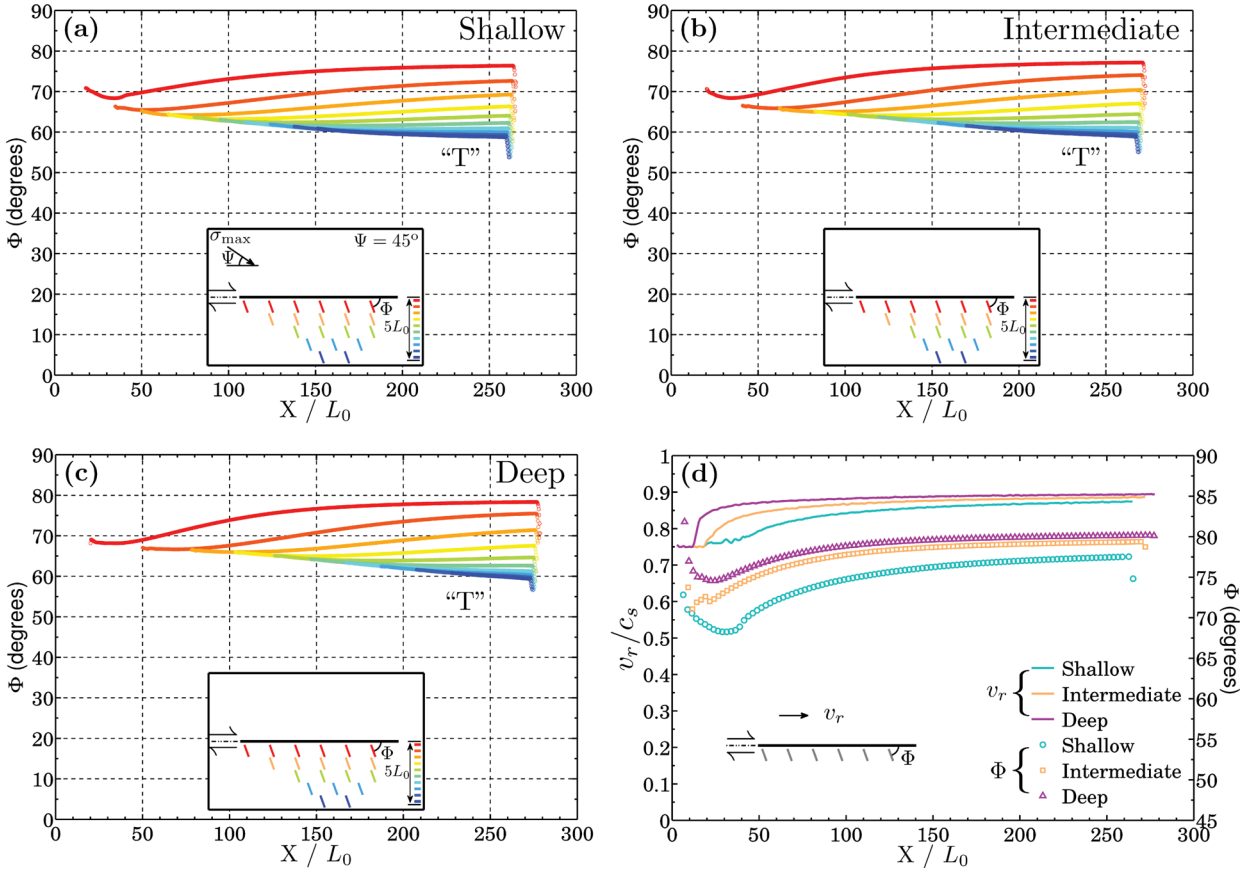

Figure 13. (a)–(c): Inferred microfracture orientation for the crack cases of Fig. 12 at different depth sections. (d) Correlation between the close-to-fault microfracture orientation and rupture speed at three typical depth sections.

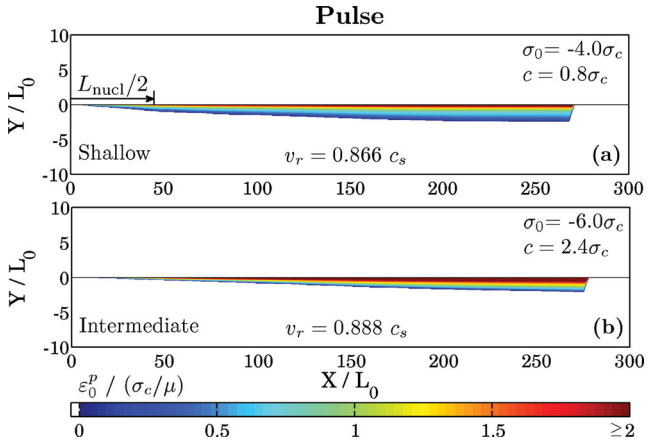

Figure 14. Plastic strain distribution for pulse-like ruptures at conditions representing different depth sections without material contrast across the fault. For both cases, $\tau_0/(-\sigma_0) = 0.26$ or $S = 2.125$. Parameters for different depth sections are: (a) $\sigma_0 = -4.0\sigma_c$, $c = 0.8\sigma_c$; (b) $\sigma_0 = -6.0\sigma_c$, $c = 2.4\sigma_c$.

Except for the variable value of γ, all other parameters are the same as in Section 2.4.1.

Starting with crack type ruptures, we find that with variable γ the slip velocity profiles still show some asymmetry with respect to the epicentre (similar to the results in Fig. 7b), while the slip profiles and overall distribution of off-fault yielding zone have a weak asymmetry with respect to the epicentre. The yielding zone thickness linearly scales with the rupture distance at each depth, with a mildly higher growth rate in the positive direction, and it systematically decreases with depth for each propagation direction (Fig. 16). The inferred angle Φ has a slightly higher average value on the compliant side than on the stiff side over the same fault normal distance range; this asymmetry becomes weaker with depth (Fig. 17). Therefore, such cases are not expected to produce clear asymmetric signals (co-seismic slip profiles and generated yielding zones) that may be observed in geological studies. One may expect that the cumulative effect of such cases with different hypocentre locations will produce damage zones with a weak asymmetry across the fault at shallow depth, and with almost symmetric distribution at deeper sections.

The corresponding results for pulse cases exhibit stronger differences for conditions representing different depth sections of bimaterial faults. As shown in Fig. 18(a), although the pulse rupture manages to propagate bilaterally for the shallow depth case (compare with the reference case in Fig. 9b), the asymmetry of the distributed yielding zone with respect to the hypocentre is still strong. In the positive direction the pulse is associated with faster rupture speed and growing yielding zone thickness, while in the negative direction it has slower rupture speed and more localized off-fault yielding zone with an approximately constant thickness. The difference in yielding zone thickness at $X = \pm 220L_0$ can be up to a factor two and seems to continue to increase with propagation distance. Similarly, the asymmetry in the local microfracture orientation with respect to the hypocentre is also prominent. The inferred angle Φ has a higher average value and a smaller standard deviation

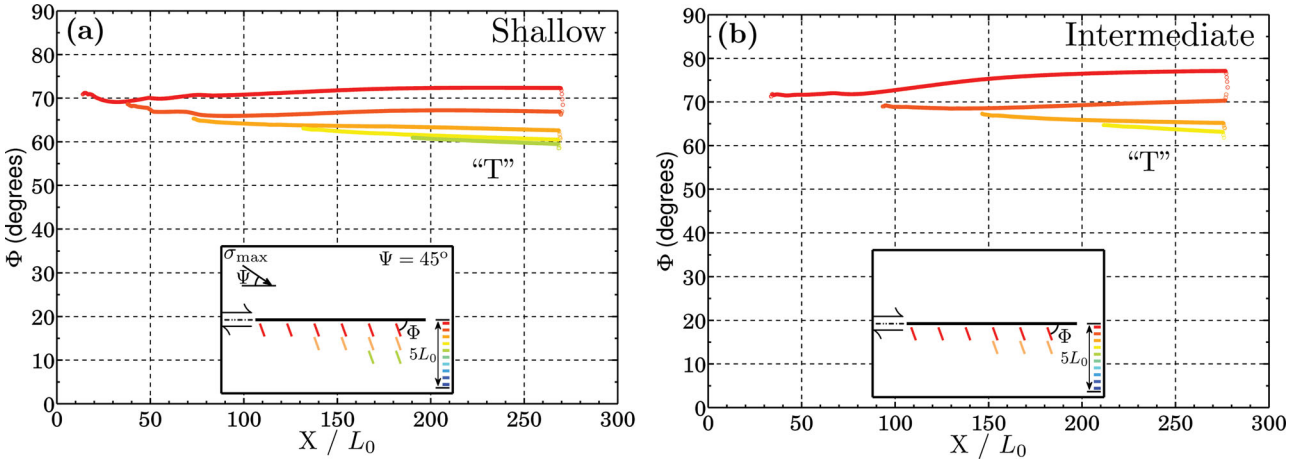

Figure 15. Inferred microfracture orientation for the pulse cases of Fig. 14 at different depth sections.

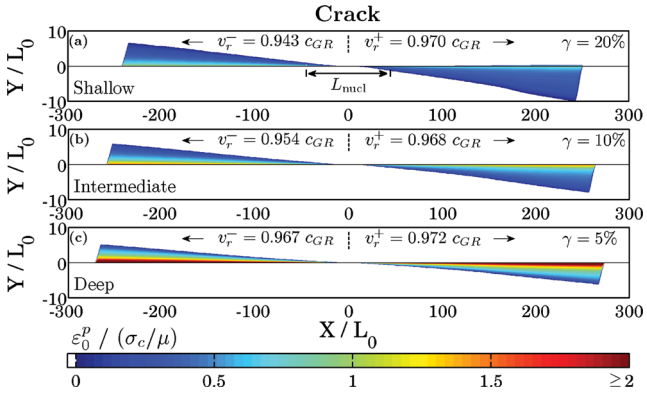

Figure 16. Plastic strain distribution for crack-like ruptures at conditions representing different depth sections on a bimaterial interface. Except for the variable degree of material contrast, all the other parameters are as in Fig. 12. Parameters for material contrast at different depth sections are: (a) $\gamma = 20$ per cent, $c_{GR} = 0.825 c_s^{fast}$; (b) $\gamma = 10$ per cent, $c_{GR} = 0.873 c_s^{fast}$; (c) $\gamma = 5$ per cent, $c_{GR} = 0.896 c_s^{fast}$.

on the more compliant side than on the stiffer side (Fig. 19a). For conditions representing intermediate depth, the asymmetries of the yielding zone thickness and local Φ are highly reduced (Figs 18b and 19b). The cumulative effect of multiple pulse-type ruptures on different depth sections of a bimaterial fault is expected to produce a relatively wide-spread damage zone at shallow depth mainly on the stiff side, and a highly localized relatively symmetric damage zone at greater depth. This is generally consistent with the simulation results of Ben-Zion & Shi (2005).

3 DISCUSSION

As discussed and reviewed by various authors (e.g. Ben-Zion & Sammis 2003; Wilson *et al.* 2003; Mitchell & Faulkner 2009; Yamashita 2009), there are many proposed fault models for the formation and development of fault zone structures. Although these models generally agree on the overall structure and elements of active fault zones (e.g. principal plane, fault core, damage zone), they may be distinguished at different spatio-temporal scales (e.g. width and functional form where inelastic deformation is non-zero, single versus many ruptures, co-seismic versus inter-seismic periods) and by some damage features that are specific to certain mechanical processes. In the following subsections we attempt to synthesize (Table 3) the findings from our parameter-space study on different characteristics of yielding zones with theoretical and observational results of others.

3.1 On faulting processes

The mechanism of generating off-fault yielding zones in our study, by rapid progression of an earthquake rupture tip along a pre-existing fault plane, is referred to as the 'fifth model' by Mitchell & Faulkner (2009). This is the dynamic counterpart to their 'third model' where off-fault damage is produced by the formation and migration of a 'process zone' around the tips of a quasi-statically growing fault. We generally do not differentiate between these two models because they share many predictions such as asymmetrically distorted stress field around the rupture or fault tip (e.g. Vermilye & Scholz 1998; Poliakov *et al.* 2002). These models may be distinguished based on features (not simulated here) likely to be specific to dynamic ruptures such as pseudotachylytes (e.g. Wenk *et al.* 2000; Di Toro *et al.* 2005) or pulverized rocks (e.g. Dor *et al.* 2006; Doan & Billi 2011; Mitchell *et al.* 2011). More subtle features that depend on rupture speed, such as the degree of stress distortion near rupture tip reflected by the microfracture orientation, and magnitude of stress drop reflected by the off-fault extent of damage zone (e.g. Andrews 1976; Rice 1980; Sibson 1989) are highly non-unique. For simplicity, we will call both models of damage production around propagating rupture and/or fault tip the 'process zone' model (PZM) and assume that the fault plane generally remains planar.

Another fault model (referred to by Mitchell & Faulkner (2009) as the 'fourth' model) emphasizes the roughness of the fault surface and suggests that the off-fault damage is due to the stress interaction and cycling over fault irregularities during displacement (e.g. Scholz 1987; Chester & Chester 2000; Wilson *et al.* 2003; Dieterich & Smith 2009). Depending on the fault surface model (e.g. roughness, frictional properties), the resulting off-fault damage can have different attributes at different scales. For convenience, we will call this model the rough fault model (RFM). One outcome of this model is the prediction that the perturbed principal stress σ'_{max} can have higher magnitude and higher inclination angle relative to local fault surface around a restraining bend than around a releasing bend (Fig. 1b), assuming the two bends have comparable size (e.g. Chester & Fletcher 1997; Griffith *et al.* 2010). Additional mechanisms for generation of fault zone damage, referred to by Mitchell & Faulkner (2009) as the 'first' and 'second' models are, respectively, processes related to fault initiation and interaction

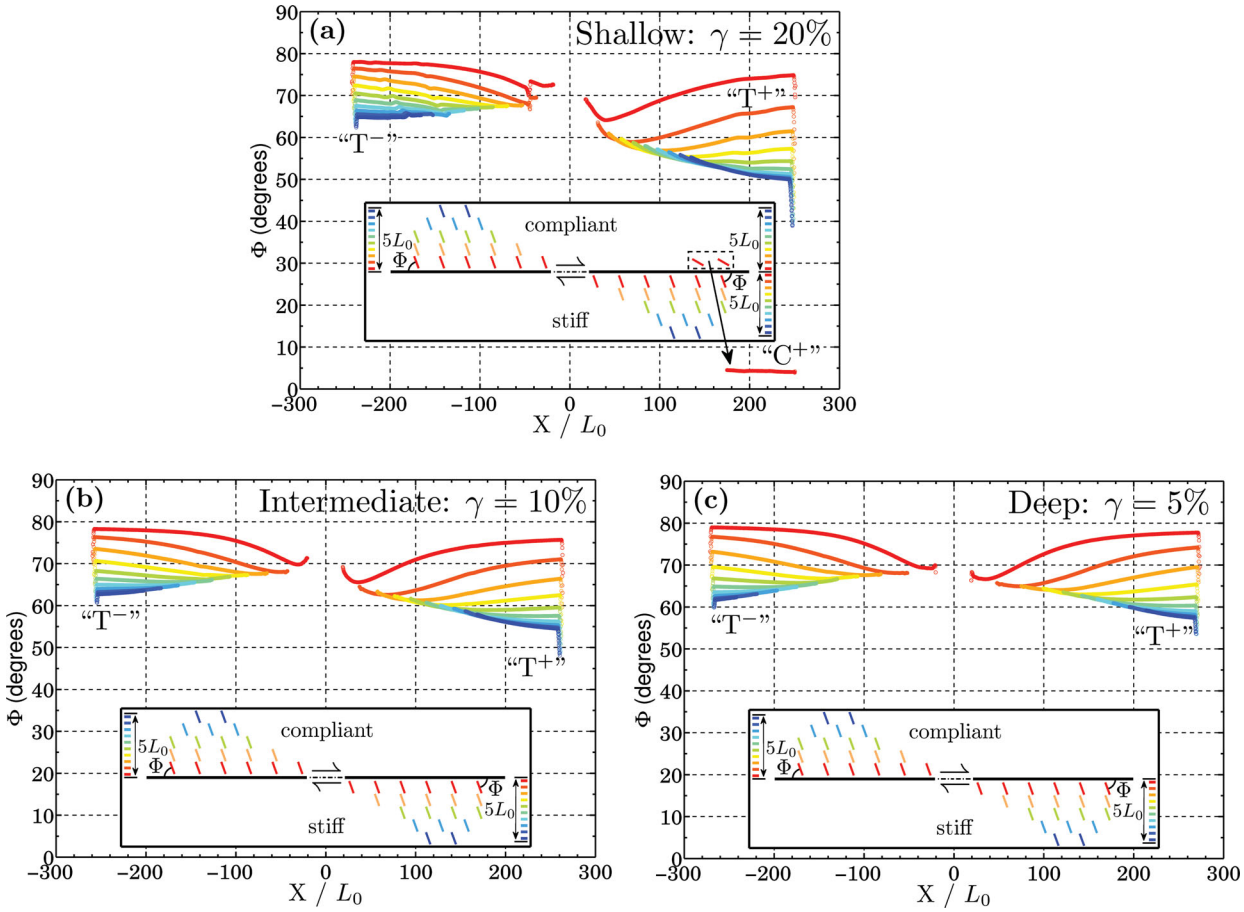

Figure 17. Inferred microfracture orientation for the crack cases of Fig. 16 at different depth sections.

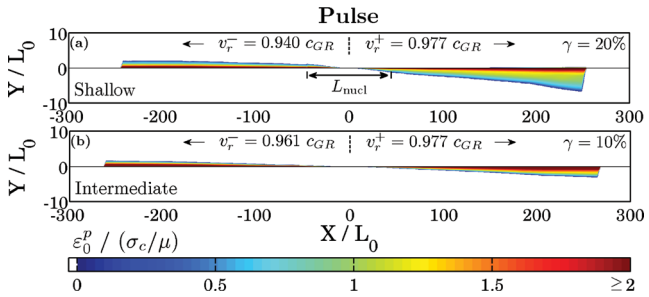

Figure 18. Plastic strain distribution for pulse-like rupture at conditions representing different depth sections on a bimaterial interface. Except for the variable degree of material contrasts, all the other parameters are as in Fig. 14. Parameters for material contrast at different depth sections are: (a) $\gamma = 20$ per cent, $c_{GR} = 0.825c_s^{\text{fast}}$; (b) $\gamma = 10$ per cent, $c_{GR} = 0.873c_s^{\text{fast}}$.

between different faults. These two processes are not considered in our following discussion.

Table 3 summarizes results on signatures of fault damage from our parameter-space study, along with expectations from other studies involving quasi-static PZM and fault motion associated with the RFM. The items listed at the top of Table 3 are various features that may be used to characterize different controlling mechanisms and the associated damage zone structure. The items listed vertically on the left give additional specifications for each fault model. The angle Ψ is assumed to be moderate to high, consistent with our focus on large strike-slip faults. A single dominant principal displacement surface in 2-D approximation is typically assumed. Damage structures involving multiple fault cores, intersection between different faults, and various 3-D effects may have features associated with superposition of the discussed entries and additional interactions not considered in this work. Various quantitative connections between faulting processes and damage structure are discussed further below.

3.2 Key signatures of PZM and RFM in yielding zones

With our assumption on relatively high Ψ and failure criteria that depend on normal stress, the PZM generally predicts for both quasi-static process and a single dynamic rupture that the off-fault yielding zone is more prominent on the extensional side of the fault (e.g. Yamashita 2000; Poliakov *et al.* 2002; Rice *et al.* 2005; Willson *et al.* 2007). This prediction is consistent with observations of asymmetrically distributed tensile cracks near the tips of shear fractures or pre-existing cuts in analogue experiments (Misra *et al.* 2009), tensile cracks along the two extensional quadrants of a small fault (Lim 1998), and tensile cracks along a frictional interface sustaining dynamic rupture in laboratory experiments (Griffith *et al.* 2009). Coupling this asymmetry with an assumed preferred propagation direction of bimaterial ruptures was used to explain the prominent damage asymmetry observed across several large strike-slip faults, with significantly more damage on the sides with faster seismic velocity at depth (e.g. Dor *et al.* 2006, 2008; Wechsler *et al.* 2009; Mitchell *et al.* 2011).

There have been suggestions that damage asymmetry may be expected also for macroscopically symmetric bilateral ruptures (Rubin

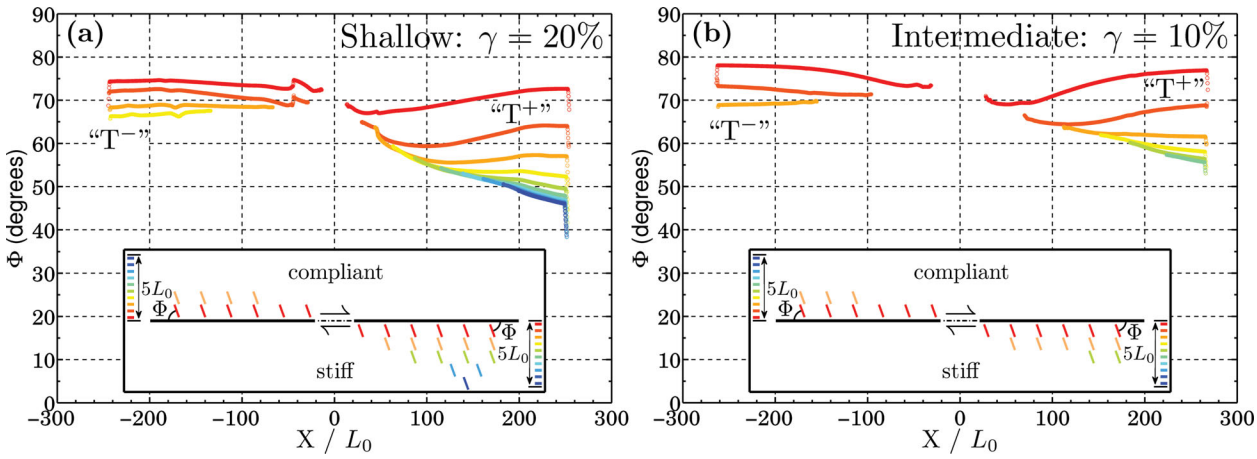

Figure 19. Inferred microfracture orientation for the pulse cases of Fig. 18.

& Ampuero 2007; Duan 2008). However, the results of DeDontney *et al.* (2011) and our study indicate that significant damage asymmetry is unlikely to be generated by macroscopically symmetric bilateral cracks for conditions representing shallow depth where the damage asymmetry has been observed. As mentioned in the introduction of Paper I, this is consistent also with results of Duan (2008) with low cohesion. Considerable damage asymmetry consistent with observations seems to require macroscopic rupture asymmetry in the form of unilateral cracks (e.g. fig. 5a of DeDontney *et al.* 2011), asymmetric bilateral pulses (e.g. this study, Fig. 19a), or unilateral pulses (e.g. fig. 5a of Ben-Zion & Shi 2005; this study, Fig. 9b). This is discussed further in Section 3.3.

The PZM also predicts that microfractures are asymmetrically oriented around the rupture or fault tips, with lower and higher angles on the compressional and extensional side, respectively. The predicted sets of microfractures for small and immature faults (related to designation 'A' in Table 3) have been observed in the field (Vermilye & Scholz 1998). For relatively large and mature faults that are seismically active (related to designation 'B' in Table 3), a mixture of predicted sets of microfractures is likely to be observed due to overprinting involving multiple rupture events nucleated at different locations. The dynamic effects of rapidly propagating ruptures, for both crack and pulse types, may modify the microfracture orientation by promoting higher inclination angle on the extensional side at higher rupture speed in the subshear regime (e.g. Poliakov *et al.* 2002; Rice *et al.* 2005). This has been observed in laboratory experiments for the rupture speed range $0.7c_R < v_r < 0.85c_R$ (Ngo *et al.* 2012), but the effect may be too subtle to observe in the field.

When considering different rupture types (crack versus pulse) of PZM, specific signatures are additionally predicted by the scaling relation between the macroscopic properties of the yielding zone (e.g. shape, thickness) and kinematic properties of the rupture (e.g. rupture length, slip and slip velocity). As mentioned, self-similar ruptures (either cracks or pulses) are expected to produce for single events triangular-shape damage zones (e.g. Andrews 2005; Templeton & Rice 2008), while nearly-steady pulse-like ruptures produce more localized damage zones with approximately constant or a slightly growing thickness (e.g. Ben-Zion & Shi 2005; Dunham *et al.* 2011a). A triangular-shape damage zone may also be produced by quasi-statically expanding cracks, and it has been observed at various positions along the trace of the Gozo fault in Maltese islands (Kim *et al.* 2004, Fig. 7a). The dynamic and quasi-static crack type faulting processes may be distinguished by the ratio of maximum damage zone thickness to crack length, if the stress drop during dynamic ruptures is usually less than that during quasi-static processes involving fracturing intact rocks (Sibson 1989). Observations of more localized damage generated by nearly steady pulse ruptures may provide information on rupture speed, stress drop and pulse width (Ben-Zion & Ampuero 2009), along with the maximum slip velocity at a position having a given yielding thickness (Ben-Zion & Shi 2005).

The general signatures of the RFM-promoted fault damage zones may be characterized by 'irregular' distribution of yielding zone properties along directions parallel or normal to the general fault strike. Nevertheless, at certain sections of the rough fault, some yielding zone properties may show correlations with the local geometric or kinematic properties of the fault. Assuming small quasi-static displacement and small amplitude-to-wavelength ratio, simple model calculations for a wavy fault with a single spectral component predict off-fault yielding that is symmetric with respect to the local fault plane and local damage extent that scales with the wavelength of the fault surface (Chester & Chester 2000). The local microfracture orientation in potential-yielding zones depends on the type of fault bend, background stress state and fault frictional properties.

For relatively weak faults with moderate to high Ψ, the perturbed stress field induced by fault roughness may produce high-angle microfractures associated with high-magnitude fault normal stress around restraining bends (designated by 'C∼' in Fig. 1(b) and Table 3), low-angle microfractures associated with possible fault opening around releasing bends (designated by 'T∼' in Fig. 1(b) and Table 3), and/or strong rotation in principal stress axes (see Fig. 1b for definition) near the convex corners of the fault (Saucier *et al.* 1992; Chester & Chester 2000; Griffith *et al.* 2010). More realistic quasi-static calculations incorporating fault roughness at many scales are expected to produce complex distribution of yielding zones along the entire fault, but not to change the basic features produced by recent failure events around each spectral component at its characteristic scale. The forgoing predictions related to fault roughness have been applied to explain the reversed sense of shear stress near the SAF in the Cajon Pass area (Saucier *et al.* 1992) and the observed fault-normal and fault-parallel microfractures along the Punchbowl fault in southern California (Wilson *et al.* 2003).

With increasing fault displacement, large-scale geometrical asperities are expected to become involved and rocks may undergo stress cycling by the juxtaposition of different irregularities of various scales and types during the change of fault configuration. This may lead to two long-term cumulative features. (1) The average yielding zone thickness is expected to scale with the total

Table 3. Observable features of fault damage zones (in 2-D approximation).

		Location	Spatial pattern and extent	Microfracture orientation†	Density decay	Scaling relation or correlation	Notes & References (this study = paper II)
PZM	Quasi-static (A&B)	in "C" (I^d&II, minor) & "T" (I^t&II, major)	T increases from the initiation point(s) towards fault growing direction (triangular shape)	$\Phi \approx 20^o$ in "C"and $\Phi \approx 70^o$ in "T"	logarithmic, expotential or power-law decay	$d_{max} \propto L$; $d_0 \propto L$; $T_{max} \propto L$; $\rho_{max} \approx$ const., indep. of L	**Crack** Cowie & Scholz (1992a), Scholz *et al.* (1993), Vermilye & Scholz (1998), Mitchell & Faulkner (2009), Savage & Brodsky (2011)
	Dynamic	A: prominently in "T" (I^t & II), might also in "C" (I^d & II) B: on both sides	A: T increases from the hypocenter towards rupture propagation direction (triangular shape), usually narrower than that for a quasi-statically growing fault B: $T \approx$ const. (moderate to wide)	A: $\Phi < \Psi$ in "C"; $\Phi > \Psi$ in "T", Φ (in "T") increases with increasing v_r ($\sim 90^o$ when v_r approaches v_{lim}) or decreasing τ_d/τ_s; sense of fault-parallel shear ahead of rupture tip can be reversed at high v_r B: two clustered sets: $\Phi < \Psi$ (minor) and $\Phi > \Psi$ (major)	logarithmic decay (A&B)	A: $d_{max} \propto L$; $T_{max}/L \propto S^{-2}$ (S is relatively large); $\rho_{max} \approx$ const., indep. of L; B: ρ_{max} grows with # of EQs (overprint[1]), might be upper bounded	**Crack** Cowie & Scholz (1992b), Scholz *et al.* (1993), Yamashita (2000), Poliakov *et al.* (2002), Andrews (2005), Templeton & Rice (2008), Ben-Zion & Ampuero (2009), Mitchell & Faulkner (2009), paper I (Figs 7, 11, 13–15), this study (Figs 2, 3–5, 12 and 13)
			A: $T \approx$ const. (narrow), can increase towards rupture propagation direction B: $T \approx$ const. (narrow to moderate)			A: d & T correlate with v_{max} and pulse width, usually approach const. but can grow with L B: overprint[1] of ρ_{max}	**Pulse** Rice *et al.* (2005), Ben-Zion & Ampuero (2009), Dunham *et al.* (2011a), paper I (Figs 7, 12, 16 and 17) this study (Figs 14 and 15)
	Dynamic + bimaterial	A: similar to the case w/o material contrast B: on both sides ("1": stiff side, "2": compliant side; "+/–" for particle motion direction on side 2/1)	similar to the case w/o material contrast (A&B), slightly-to-moderately more pronounced in "+" direction (A) or on the stiff side (B)	A: $\Phi_2^- > \Phi_1^+ > \Psi$ in "T", $\Phi < \Psi$ in "C" B: similar to the case w/o material contrast; for the majority: $\Phi_2 > \Phi_1 > \Psi$	logarithmic decay with asymmetric slopes wrt. the hypocenter (A) or across the fault (B)	A: $d^{\pm}_{max} \propto L^{\pm}$; $T^{\pm}_{max} \propto L^{\pm}$; asymmetry of T & d wrt. the hypocenter correlates with γ; B: T_1/T_2 correlates with γ	**Crack** Duan (2008), DeDontney *et al.* (2011), this study (Figs 6–8, 16 and 17)
			A: $T^+ \approx$ const. (narrow to moderate), can grow with L^+; T^- depends, usually highly localized; B: T_1 (moderate) $\gg T_2$ (localized)			A: $d^{\pm}$ & $T^{\pm}$ correlate with $v^{\pm}_{max}$; $d^+ \approx$ const., might grow with L^+; d^- depends, usually rapidly tapers B: T_1/T_2 correlates with γ	**Pulse** Ben-Zion & Shi (2005), Ampuero & Ben-Zion (2008), this study (Figs 9–11, 18 and 19)
RFM	Quasi-static	on both sides (A&B)	A: T fluctuates along strike, may be more extensive around "T∼" than around "C∼" B: $T \approx$ const.	irregular: from fault parallel to fault normal when f is not very high; sense of fault-parallel shear near convex corner can be reversed with low f (A&B)	exponential or power-law decay (A&B)	A: $d_{max} \propto \beta^{-2}$, indep. of L (L is large), $d_{max} \propto L$ (L is small); $T \propto \lambda$, $\rho_{max} \propto \lambda^{-\alpha}$ ($\alpha > 0$) B: $T \propto d$, also depends on λ_{max}; ρ_{max} grows with d (overprint[2]), might be upper bounded	**Crack** Saucier *et al* (1992), Chester & Fletcher (1997), Chester & Chester (2000), Wilson *et al.* (2003), Dieterich & Smith (2009), Griffith *et al.* (2010)
	Dynamic	A: the overall location may agree well with that predicted by PZM B: on both sides	A: T fluctuates along strike, may show patterns of PZM along portions with low β; damage may be absent in the immediate vincinity of "T∼" B: $T \approx$ const. with fluctuation	several clustered sets, which are expcted to reflect the competition between dynamic effect and local rough fault surface (A&B)	N.A. (A&B)	A: lack of macroscopic scaling relations at the present time; v_r anti-correlates with the slope of fault profile B: N.A.	**Crack/Pulse** Duan & Day (2008), Dumham *et al.* (2011b), Shi & Day (2011)

PZM = Process Zone Model (with approximately planar fault interface), RFM = Rough Fault Model. A single principal fault surface is assumed. The angle Ψ of the background maximum compressive stress relative to the fault is assumed to be moderate to high, representive for (but not limited to) large strike-slip faults.

† The orientation is described by the angle Φ of the measured (or inferred) microfractures (aligned to the mode-I type) relative to the fault.

A: in a short-term process (e.g. during a single seismic event or with small amount of displacement), B: in a long-term process (e.g. after multiple seismic cycles with variable hypocenter locations or with large cumulative displacement); "C"&"T": compressional and extensional quadrants, respectively; "C∼"&"T∼": restraining and releasing bends, respectively; I^d: dilatant microfractures (under compression), I^t: tensile microfractures (under transient tension); II: mode-II shear microfractures; T: damage zone thickness; d: displacement or seismic slip; d_0: characteristic displacement on the trailing edge of process zone; L: fault half length or rupture distance; ρ: microfracture density or its equivalence (e.g. seismic potency density); v_r: rupture speed; τ_d: dynamic shear strength of the fault; τ_s: static shear strength of the fault; S: relative strength S parameter (see the text); v_{max} : maximum slip velocity; γ: degree of material contrast; f: friction coefficient; β: roughness (e.g. rms slope) of fault profile; λ: wavelength of fault profile. Subscript "max" is used to specify the maximum value of a quantity (e.g. d_{max} , T_{max} , ρ_{max}).

© 2012 The Authors, *GJI*, **191,** 1343–1360

displacement and largest wavelength of fault roughness along the examined fault segment (Chester & Chester 2000; Savage & Brodsky 2011). (2) An overprinting of microfractures is expected to produce a mixture of low- and high-angle microfractures at an arbitrary location inside the yielding zone, and the maximum microfracture density is expected to correlate with the fault displacement (Wilson *et al.* 2003; Mitchell & Faulkner 2009).

All models predict a decay of microfracture density with distance from the principal fault surface. The results of this study indicate that the functional form of the decay is logarithmic over most of the yielding zone extent (e.g. Fig. 3), consistent with the numerical study of Yamashita (2000). In contrast, Dieterich & Smith (2009) suggested based on quasi-static simulations of slip on a rough fault a power law decay of damage with distance from the fault. Some studies on quasi-static deformation of a wavy fault had an exponential component in the solution for the decay of the perturbed stress field from the fault (Saucier *et al.* 1992; Chester & Chester 2000), suggesting exponential damage decay in locations where this component dominates the full solution. The functional forms used to fit field observations vary in different studies. Vermilye & Scholz (1998) fitted microfracture density decay for several small faults in New York State with a logarithmic form. Mitchell *et al.* (2011) used the logarithmic form to fit the reduction of rock pulverization intensity with distance from the main slip surface of the Arima-Takatsuki Tectonic line in Japan. Savage & Brodsky (2011) used a power law to fit fracture density decay for small faults near Santa Cruz, California. Mitchell & Faulkner (2009) used an exponential decay form for the Atacama fault zone in northern Chile. The difference in fitting functions may stem from a preference related to assumed models or intended use, or it may reflect actual differences in the key operating processes associated with the different examined locations.

3.3 Mechanisms for damage generation off a bimaterial fault

Several effects can contribute to asymmetric off-fault damage distribution produced by multiple earthquake ruptures on a planar bimaterial fault. The opposite senses of normal stress changes near the rupture tips propagating in the opposite directions can lead to the development of unidirectional pulse or bilateral rupture with asymmetric slip and rupture velocities (e.g. Shi & Ben-Zion 2006; Ampuero & Ben-Zion 2008; Brietzke *et al.* 2009). Since damage is promoted on the extensional side for cases with high Ψ representing large strike slip faults, ruptures that are unilateral or more pronounced in one direction, will produce asymmetric damage across the fault.

As shown in Figs 6–7 and 9–10 and by DeDontney *et al.* (2011), in cases with high Ψ the coupling of off-fault energy dissipation due to yielding contributes to the asymmetry of bimaterial ruptures compared to purely elastic cases. (In cases with low Ψ representing thrust faults, the off-fault energy dissipation can produce opposite rupture asymmetry). The combined result is expected to produce for subshear ruptures on large strike-slip faults a statistically preferred propagation in the positive direction (Fig. 1a), associated with more prominent damage on the stiff side. The type of damage generated may be shear, tensile, or a mixture of both, depending on the adopted criteria and competition between different failure modes. We note that although in some studies the elastically predicted or modelled plastic strain is a shear type failure, its generation in some regions may be associated with tensile stress or normal stress close to tensile (e.g. Andrews & Ben-Zion 1997; Ben-Zion & Huang 2002; Dalguer & Day 2009). Therefore this type of damage may be used as an indicator for potential tensile stress, at least for some locations on the extensional side and along the fault right behind the rupture tip in the positive direction (Duan 2008).

Some damage asymmetry across a bimaterial interface can also be produced under quasi-static loadings. This has been invoked to explain asymmetric tensile micro-cracking near grain boundaries separating different minerals (e.g. Dey & Wang 1981; Kranz 1983). However, in such cases involving approximately planar boundaries the damage is confined to the immediate vicinity of the interface. In cases of large bimaterial faults with roughness, more extensive damage with potential tensile cracking may occur quasi-statically during the interseismic period around releasing bends (e.g. Chester & Chester 2000). However, this is expected to be dominated by the roughness and hence produce approximately symmetric damage.

A related topic is the observation of pulverized rocks along several large strike-slip faults (e.g. Dor *et al.* 2006, 2008; Mitchell *et al.* 2011). The pulverized rocks were found to be strongly asymmetric with respect to the main slip zone, with most pulverized rock bodies on the side with faster seismic velocity at depth. The damage asymmetry documented in these studies extends over hundreds of metres, and has been observed in places to be accompanied by across-fault asymmetry over several km involving various geomorphic features (e.g. Dor *et al.* 2008; Wechsler *et al.* 2009). Several signatures of the observed pulverized rocks suggest that they are produced under conditions associated with tensile stress (see Mitchell *et al.* 2011, and references therein). Experimental studies suggest that generation of pulverized rocks require high dynamic strain rates (Doan & Gary 2009; Doan & Billi 2011).

The wide extent of the observed pulverized rocks, their observations in the context of large bimaterial strike-slip faults and their existence primarily on the side with faster velocity at depth suggest that they are likely produced by repeated predominantly unilateral or strongly asymmetric bilateral ruptures. Based on the results of Sections 2.3 and 2.4.2 that weakly asymmetric ruptures are not expected to produce significant damage asymmetry in low cohesion materials typical of shallow depths and previous related studies, we may conclude that strongly asymmetric fault zone damage that includes pulverized rocks is likely generated by pulse-type ruptures with statistically preferred propagation direction, although we cannot exclude the unilateral or strongly asymmetric crack-type ruptures (see discussion in Section 3.2).

3.4 Limitations of the presented results and potential future improvements

We have used 2-D simulations to explore changes of fault zone damage with depth that is likely generated by dynamic ruptures. Our 2-D simulations with the adopted Mohr-Coulomb criterion do not account for the stress/strength gradient with depth (Ma & Andrews 2010), the effect of the intermediate principal stress in influencing rock damage (Lockner & Beeler 2002), the finite width of the seismogenic zone and the free surface (Day 1982; Ma & Andrews 2010). In particular, the finite seismogenic depth implies an upper limit on self-similar rupture growth (Day 1982). Concerning our results about the evolution of the plastic zone thickness for self-similar and quasi-steady ruptures, this suggests that the extent of the damage zone scales linearly with fault length up to a value proportional to the seismogenic depth. More precisely, our results for $\Psi = 45^\circ$ (Fig. 4) imply that the fault zone thickness saturates at a value of a few per cent the seismogenic depth, which is a few hundred metres. This provides a possible explanation for the

observation that fault zone thickness for faults with large cumulative slip is typically a few hundred metres, independently of fault length (Mitchell & Faulkner 2009; Savage & Brodsky 2011).

Our 2-D simulations do not properly reflect the sensitivity of the Green's function to a local disturbance in 3-D (Evans 1998, chapter 2.4). Moreover, we have adopted a simple setting of model parameters without introducing saturation of the effective normal stress at some depth or implied scaling relation of the slip-weakening distance with final slip (e.g. Rice 1993; Abercrombie & Rice 2005), nor did we consider effects associated with pre-existing low velocity fault zone layer (e.g. Harris & Day 1997; Ben-Zion & Huang 2002; Huang & Ampuero 2011). These limitations could accordingly affect our evaluation of the 3-D structure of fault damage zones. Given that many adopted yielding criteria in both 2-D and 3-D are pressure dependent (e.g. Templeton & Rice 2008; Ma & Andrews 2010) and the size of potential off-fault failure zone may scale with the slip-weakening distance (Rice *et al.* 2005), our results should be augmented by a future parameter-space study using 3-D simulations of crack- and pulse-like ruptures.

Only limited numerical simulations of dynamic ruptures along rough faults have been performed so far, mainly with a focus on high-frequency radiation and basic properties of off-fault yielding (e.g. Dunham *et al.* 2011b; Shi & Day 2011). As indicated in Table 3 for this category, there are many yielding zone properties that are not covered or explored by these studies, such as the competition between properties of dynamic ruptures and generated yielding zones. Some results of dynamic rupture models show no or little damage in the immediate vicinity of fault releasing bends (Dunham *et al.* 2011b, Fig. 3c) or fault kink that is oriented into the extensional quadrant (Duan & Day 2008, Fig. 13), in contrast to the quasi-static expectations for a wavy fault (Chester & Chester 2000). These and other issues should be clarified by future simulations of ruptures on rough faults.

The simulations done in this study and related earlier works used off-fault yielding in the form of plastic strain, rather than brittle damage as observed geologically (e.g. Wilson *et al.* 2003; Dor *et al.* 2008; Mitchell & Faulkner 2009) and seismologically (e.g. Lewis *et al.* 2005; Allam & Ben-Zion 2012) in the structure of natural faults. Brittle damage is associated with permanent volumetric changes (e.g. Jaeger *et al.* 2007), and the reduction of elastic moduli in the damage zones can lead to significant motion amplification (e.g. Spudich & Olsen 2001; Peng & Ben-Zion 2006) and additional dynamic feedback mechanisms not accounted for by plasticity. Examining the effects of such mechanisms, and producing clearer predictions on damage products that may be compared with *in-situ* observations, require simulations that incorporate brittle damage. This will be done in a follow up work.

ACKNOWLEDGMENTS

We thank Massimo Cocco, an anonymous referee and Editor Xiaofei Chen for useful comments. The study was supported by the National Science Foundation (grants EAR-0944066 and EAR-0908903) and the Southern California Earthquake Center (based on NSF Cooperative Agreement EAR-0529922 and USGS Cooperative Agreement 07HQAC0026).

REFERENCES

Abercrombie, R.E. & Rice, J.R., 2005. Can observations of earthquake scaling constrain slip weakening?, *Geophys. J. Int.,* **162,** 406–424.

Allam, A.A. & Ben-Zion, Y., 2012. Seismic velocity structures in the Southern California plate-boundary environment from double-difference tomography, *Geophys. J. Int.,* **190,** 1181–1196, doi:10.1111/j.1365-246X.2012.05544.x.

Ampuero, J.-P. & Ben-Zion, Y., 2008. Cracks, pulses and macroscopic asymmetry of dynamic rupture on a bimaterial interface with velocity-weakening friction, *Geophys J. Int.,* **173,** 674–692, doi:10.1111/j.1365-246X.2008.03736.x.

Andrews, D.J., 1976. Rupture velocity of plane strain shear cracks, *J. geophys. Res.,* **81,** 5679–5687.

Andrews, D.J., 2005. Rupture dynamics with energy loss outside the slip zone, *J. geophys. Res.,* **110,** B01307, doi:10.1029/2004JB003191.

Andrews, D.J. & Ben-Zion, Y., 1997. Wrinkle-like slip pulse on a fault between different materials, *J. geophys. Res.,* **102,** 553–571.

Ben-Zion, Y., 1990. The response of two half spaces to point dislocations at the material interface, *Geophys. J. Int.,* **101,** 507–528.

Ben-Zion, Y. & Ampuero, J.-P., 2009. Seismic radiation from regions sustaining material damage, *Geophys. J. Int.,* **178,** 1351–1356, doi:10.1111/j.1365-246X.2009.04285.x.

Ben-Zion, Y. & Huang, Y., 2002. Dynamic rupture on an interface between a compliant fault zone layer and a stiffer surrounding solid, *J. geophys. Res.,* **107**(B2), 2042, doi:10.1029/2001JB000254.

Ben-Zion, Y. & Sammis, C.G., 2003. Characterization of fault zones, *Pure appl. Geophys.,* **160,** 677–715.

Ben-Zion, Y. & Shi, Z., 2005. Dynamic rupture on a material interface with spontaneous generation of plastic strain in the bulk, *Earth planet. Sci. Lett.,* **236,** 486–496, doi:10.1016/j.epsl.2005.03.025.

Ben-Zion, Y. *et al*., 2003. Shallow fault zone structure illuminated by trapped waves in the Karadere-Duzce branch of the North Anatolian Fault, western Turkey, *Geophys. J. Int.,* **152,** 699–717.

Brietzke, G.B., Cochard, A. & Igel, H., 2009. Importance of biomaterial interfaces for earthquake dynamics and strong ground motion, *Geophys. J. Int.,* **178**(2), 921–938.

Broberg, K.B., 1999. *Cracks and Fracture,* Academic Press, San Diego, CA.

Chester, F.M. & Chester, J.S., 2000. Stress and deformation along wavy frictional faults, *J. geophys. Res.,* **105**(B10), 23 421–23 430.

Chester, J.S. & Fletcher, R.C., 1997. Stress distribution and failure in anisotropic rock near a bend on a weak fault, *J. geophys. Res.,* **102**(B1), 693–708, doi:10.1029/96JB02791.

Cowie, P.A. & Scholz, C.H., 1992a. Physical explanation for the displacement-length relationship of faults using a post-yielding fracture mechanics model, *J. Struct. Geol.,* **14**(10), 1133–1148.

Cowie, P.A. & Scholz, C.H., 1992b. Growth of Faults by Accumulation of Seismic Slip, *J. geophys. Res.,* **97**(B7), 11 085–11 095, doi:10.1029/92JB00586.

Dalguer, L.A. & Day, S.M., 2009. Asymmetric rupture of large aspect-ratio faults at bimaterial interface in 3D, *Geophys. Res. Lett.,* **36,** L23307, doi:10.1029/2009GL040303.

Das, S. & Aki, K., 1977. A numerical study of two-dimensional spontaneous rupture propagation, *Geophys. J. R. astr. Soc.,* **50**(3), 643–668, doi:10.1111/j.1365-246X.1977.tb01339.x

Day, S.M., 1982. Three-dimensional finite difference simulation of fault dynamics: rectangular faults with fixed rupture velocity, *Bull. seism. Soc. Am.,* **72,** 705–727

DeDontney, N., Templeton-Barrett, E.L., Rice, J.R. & Dmowska, R., 2011. Influence of plastic deformation on bimaterial fault rupture directivity, *J. geophys. Res.,* **116,** B10312, doi:10.1029/2011JB008417.

Dey, T.N. & Wang, C-Y., 1981. Some mechanisms of microcrack growth and interaction in compressive rock failure, *Int. J. Rock Mech. Min. Sci.,* **18,** 199–209.

Dieterich, J.H. & Smith, D.E., 2009. Nonplanar faults: mechanics of slip and off-fault damage, *Pure appl. Geophys.,* **166**(10), 1799–1815, doi:10.1007/s00024-009-0517-y.

Di Toro, G., Nielsen, S. & Pennacchioni, G., 2005. Earthquake rupture dynamics frozen in exhumed ancient faults, *Nature,* **436,** 1009–1012, doi:10.1038/nature03910.

Doan, M.-L. & Billi, A., 2011. High strain rate damage of Carrara marble, *Geophys. Res. Lett.,* **38,** L19302, doi:10.1029/2011GL049169

Doan, M.L. & Gary, G., 2009. Rock pulverization at high strain rate near the San Andreas Fault, *Nat. Geosci.,* **2,** 709–712, doi:10.1038/ngeo640.

Dor, O., Ben-Zion, Y., Rockwell, T.K. & Brune, J.N., 2006. Pulverized Rocks in the Mojave section of the San Andreas FZ, *Earth planet. Sci. Lett.,* **245,** 642–654, doi:10.1016/j.epsl.2006.03.034.

Dor, O., Yildirim, C., Rockwell, T.K., Ben-Zion, Y., Emre, O., Sisk, M. & Duman, T.Y., 2008. Geologic and geomorphologic asymmetry across the rupture zones of the 1943 and 1944 earthquakes on the North Anatolian Fault: possible signals for preferred earthquake propagation direction, *Geophys. J. Int.,* **173,** 483–504, doi:10.1111/j.1365-246X.2008.03709.x.

Duan, B., 2008. Asymmetric off-fault damage generated by bilateral ruptures along a bimaterial interface, *Geophys. Res. Lett.,* **35,** L14306, doi:10.1029/2008GL034797.

Duan, B. & Day, S.M., 2008. Inelastic strain distribution and seismic radiation from rupture of a fault kink, *J. geophys. Res.,* **113,** B12311, doi:10.1029/2008JB005847.

Dunham, E.M., Belanger, D., Cong, L. & Kozdon, J.E., 2011a. Earthquake ruptures with strongly rate-weakening friction and off-fault plasticity, 1: planar faults, *Bull. seism. Soc. Am.,* **101**(5), 2296–2307, doi:10.1785/0120100075.

Dunham, E.M., Belanger, D., Cong, L. & Kozdon, J.E., 2011b. Earthquake ruptures with strongly rate-weakening friction and off-fault plasticity, 2: nonplanar faults, *Bull. seism. Soc. Am.,* **101**(5), 2308–2322, doi:10.1785/0120100076.

Evans, L.C., 1998. *Partial Differential Equations,* American Mathematical Society, Providence, RI.

Freund, L.B., 1990. *Dynamic Fracture Mechanics,* Cambridge University Press, New York, NY.

Griffith, W.A., Nielsen, S., Di Toro, G. & Smith, S.A.F., 2010. Rough faults, distributed weakening, and off-fault deformation, *J. geophys. Res.,* **115,** B08409, doi:10.1029/2009JB006925.

Griffith, W.A., Rosakis, A.J., Pollard, D.D. & Ko, C.-W., 2009. Dynamic rupture experiments elucidate tensile crack development during propagating earthquake ruptures, *Geology,* **37,** 795–798, doi:10.1130/G30064A.

Harris, R.A. & Day, S.M., 1997. Effects of a low-velocity zone on a dynamic rupture, *Bull. seism. Soc. Am.,* **87,** 1267–1280.

Huang, Y. & Ampuero, J.-P., 2011. Pulse-like ruptures induced by low-velocity fault zones, *J. geophys. Res.,* **116,** B12307, doi:10.1029/2011JB008684.

Jaeger, J., Cook, N. & Zimmerman, R., 2007. *Fundamentals of Rock Mechanics,* 4th edn, Blackwell Publishing Ltd, Malden, MA.

Johnson, P.A. & Jia, X., 2005. Nonlinear dynamics, granular media and dynamic earthquake triggering, *Nature,* **473,** 871–874.

Kaneko, Y. & Fialko, Y., 2011. Shallow slip deficit due to large strike-slip earthquakes in dynamic rupture simulations with elasto-plastic off-fault response, *Geophys. J. Int.,* **186,** 1389–1403, doi:10.1111/j.1365-246X.2011.05117.x.

Kim, Y.-S., Peacock, D.C.P. & Sanderson, D.J., 2004. Fault damage zones, *J. Struct. Geol.,* **26,** 503–517.

Kranz, R.L., 1983. Microcracks in rocks: a review, *Tectonophysics,* **100,** 449–480.

Le Pichon, X., Kreemer, C. & Chamot-Rooke, N., 2005. Asymmetry in elastic properties and the evolution of large continental strike-slip faults, *J. geophys. Res.,* **110,** B03405, doi:10.1029/2004JB003343.

Lewis, M.A. & Ben-Zion, Y., 2010. Diversity of fault zone damage and trapping structures in the Parkfield section of the San Andreas Fault from comprehensive analysis of near fault seismograms, *Geophys. J. Int.,* **183,** 1579–1595, doi:10.1111/j.1365-246X.2010.04816.x.

Lewis, M.A., Peng, Z., Ben-Zion, Y. & Vernon, F.L., 2005. Shallow seismic trapping structure in the San Jacinto fault zone near Anza, California, *Geophys. J. Int.,* **162,** 867–881.

Lewis, M.A, Ben-Zion, Y. & McGuire, J., 2007. Imaging the deep structure of the San Andreas Fault south of Hollister with joint analysis of fault-zone head and direct P arrivals, *Geophys. J. Int.,* **169,** 1028–1042, doi:10.1111/j.1365-246X.2006.03319.x.

Lim, S.J., 1998. Small strike slip faults in granitic rock: implications for three dimensional models, *Masters thesis*, Utah State University, Logan, UT.

Lockner, D.A. & Beeler, N.M., 2002. Rock failure and earthquakes, in *International Handbook of Earthquake and Engineering Seismology,* pp. 505–537, eds Lee, W.H.K., Kanamori, H., Jennings, P.C. & Kisslinger, C., Academic Press, Amsterdam.

Ma, S., 2008. A physical model for widespread near-surface and fault zone damage induced by earthquakes, *Geochem. Geophys. Geosyst.,* **9,** Q11009, doi:10.1029/2008GC002231.

Ma, S. & Andrews, D.J., 2010. Inelastic off-fault response and three-dimensional dynamics of earthquake rupture on a strike-slip fault, *J. geophys. Res.,* **115,** B04304, doi:10.1029/2009JB006382.

McGuire, J. & Ben-Zion, Y., 2005. High-resolution imaging of the Bear Valley section of the San Andreas Fault at seismogenic depths with fault-zone head waves and relocated seismicity, *Geophys. J. Int.,* **163,** 152–164, doi:10.1111/j.1365-246X.2005.02703.x.

Misra, S., Mandal, N., Dhar, R. & Chakraborty, C., 2009. Mechanisms of deformation localization at the tips of shear fractures: findings from analogue experiments and field evidence, *J. geophys. Res.,* **114,** B04204, doi:10.1029/2008JB005737.

Mitchell, T.M. & Faulkner, D.R., 2009. The nature and origin of off-fault damage surrounding strike-slip fault zones with a wide range of displacements: a field study from the Atacama fault system, northern Chile, *J. Strutc. Geol.,* **31,** 802–816.

Mitchell, T.M., Ben-Zion, Y. & Shimamoto, T., 2011. Pulverized fault rocks and damage asymmetry along the Arima-Takatsuki Tectonic Line, Japan, *Earth planet. Sci. Lett.,* **308,** 284–297, doi:10.1016/j.epsl.2011.04.023.

Ngo, D., Huang, Y., Rosakis, A.J., Griffith, W.A. & Pollard, D.D., 2012. Off-fault tensile cracks: a link between geological fault observations, lab experiments and dynamic rupture models, *J. geophys. Res.,* B01307, doi:10.1029/2011JB008577.

Nielsen, S.B. & Carlson, J.M., 2000. Rupture pulse characterization: self-healing, self-similar, expanding solutions in a continuum model of fault dynamics, *Bull. seism. Soc. Am.,* **90,** 1480–1497.

Oglesby, D.D., Mai, P.M., Atakan, K. & Pucci, S., 2008. Dynamic models of earthquakes on the North Anatolian fault zone under the Sea of Marmara: effect of hypocenter location, *Geophys. Res. Lett.,* **35,** L18302, doi:10.1029/2008GL035037.

Palmer, A.C. & Rice, J.R., 1973. Growth of slip surfaces in progressive failure of over-consolidated clay, *Proc. R. Soc. London, Ser. A.,* **332,** 527–548.

Peng, Z. & Ben-Zion, Y., 2006. Temporal changes of shallow seismic velocity around the Karadere-Düzce branch of the North Anatolian Fault and strong ground motion, *Pure appl. Geophys.,* **163,** 567–600, doi:10.1007/s00024-005-0034-6.

Poliakov, A.N.B., Dmowska, R. & Rice, J.R., 2002. Dynamic shear rupture interactions with fault bends and off-axis secondary faulting, *J. geophys. Res.,* **107,** doi:10.1029/2001JB000572.

Rockwell, T.K. & Ben-Zion, Y., 2007. High localization of primary slip zones in large earthquakes from paleoseismic trenches: observations and implications for earthquake physics, *J. geophys. Res.,* **112,** B10304, doi:10.1029/2006JB004764.

Rice, J.R., 1980. The mechanics of earthquake rupture, in *Physics of the Earth's Interior,* pp. 555–649. eds Dzieswonski, A.M. & Boschi, E., Italian Physical Society/North Holland, Amsterdam.

Rice, J.R., 1993. Spatio-temporal complexity of slip on a fault, *J. geophys. Res.,* **98**(B6), 9885–9907, doi:10.1029/93JB00191.

Rice, J.R., Sammis, C.G. & Parsons, R., 2005. Off-fault secondary failure induced by a dynamic slip-pulse, *Bull. seism. Soc. Am.,* **95**(1), 109–134, doi:10.1785/0120030166.

Rubin, A.M. & Ampuero, J.-P., 2007. Aftershock asymmetry on a bimaterial interface, *J. geophys. Res.,* **112,** B05307, doi:10.1029/2006JB004337.

Saucier, F., Humphreys, E. & Weldon, II, R., 1992. Stress near geometrically complex strike-slip faults: application to the San Andreas Fault at Cajon Pass, Southern California, *J. geophys. Res.,* **97**(B4), 5081–5094, doi:10.1029/91JB02644.

Savage, H.M. & Brodsky, E.E., 2011. Collateral damage: evolution with displacement of fracture distribution and secondary fault strands in fault damage zones, *J. geophys. Res.,* **116,** B03405, doi:10.1029/2010JB007665.

Scholz, C.H., 1987. Wear and gouge formation in brittle faulting, *Geology,* **15,** 493–495.

Scholz, C.H., 2002. *The Mechanics of Earthquakes and Faulting,* Cambridge Univ. Press, New York, NY.

Scholz, C.H., Dawers, N.H., Yu, J.-Z., Anders, M.H. & Cowie, P.A., 1993. Fault growth and fault scaling laws: preliminary results, *J. geophys. Res.,* **98**(B12), 21951–21961, doi:10.1029/93JB01008.

Shi, Z. & Ben-Zion, Y., 2006. Dynamic rupture on a bimaterial interface governed by slip-weakening friction, *Geophys. J. Int.,* **165,** 469–484.

Shi, Z. & Day, S.M., 2011. 3D simulations of dynamic rupture on rough faults, *EOS, Trans. Am. geophys. Un.,* **92,** Abstract S54C-06.

Shi, Z., Ben-Zion, Y. & Needleman, A., 2008. Properties of dynamic rupture and energy partition in a solid with a frictional interface, *J. Mech. Phys. Solids,* **56,** 5–24.

Sibson, R.H., 1989. Earthquake faulting as a structural process, *J. Strutc. Geol.,* **11,** 1–14.

Spudich, P. & Olsen, K.B., 2001. Fault zone amplified waves as a possible seismic hazard along the Calaveras Fault in central California, *Geophys. Res. Lett.,* **28**(13), 2533–2536, doi:10.1029/2000GL011902.

Templeton, E.L. & Rice, J.R., 2008. Off-fault plasticity and earthquake rupture dynamics: 1. dry materials or neglect of fluid pressure changes, *J. geophys. Res.,* **113,** B09306, doi:10.1029/2007JB005529.

Thurber, C., Zhang, H., Waldhauser, F., Hardebeck, J., Micheal, A. & Eberhart-Phillips, D., 2006. Three-dimensional compressional wavespeed model, earthquake relocations, and focal mechanisms for the Parkfield, California, region, *Bull. seism. Soc. Am.,* **96**(4B), S38–S49.

Vermilye, J.M. & Scholz, C.H., 1998. The process zone: a microstructural view of fault growth, *J. geophys. Res.,* **103,** 12 223–12 237, doi:10.1029/98JB00957.

Wechsler, N., Rockwell, T.K. & Ben-Zion, Y., 2009. Analysis of rock damage asymmetry from geomorphic signals along the trifurcation area of the San-Jacinto Fault, *Geomorphology,* **113,** 82–96.

Wenk, H.-R., Johnson, L.R. & Ratschbacher, L., 2000. Pseudotachylites in the eastern Peninsular ranges of California, *Tectonophysics,* **321,** 253–277.

Willson, J.P., Lunn, R.J. & Shipton, Z.K., 2007. Simulating spatial and temporal evolution of multiple wing cracks around faults in crystalline basement rocks, *J. geophys. Res.,* **112,** B08408, doi:10.1029/2006JB004815.

Wilson, J.E., Chester, J.S. & Chester, F.M., 2003. Microfracture analysis of fault growth and wear processes, Punchbowl Fault, San Andreas System, California, *J. Struct. Geol.,* **25,** 1855–1873.

Xu, S., Ben-Zion, Y. & Ampuero, J.-P., 2012. Properties of inelastic yielding zones generated by in-plane dynamic ruptures—I. Model description and basic results, *Geophys. J. Int.,* in press, doi:10.1111/j.1365-246X.2012.05679.x (this issue).

Yamashita, T., 2000. Generation of microcracks by dynamic shear rupture and its effects on rupture growth and elastic wave radiation, *Geophys. J. Int.,* **143,** 395–406.

Yamashita, T., 2009. Chapter 8: Rupture dynamics on bimaterial faults and nonlinear off-fault damage, in *Fault-Zone Properties and Earthquake Rupture Dynamics,* Int. geophys. Ser. 94, pp. 187–215, ed. Fukuyama, E., Academic Press, San Diego, CA.

Yang, H. & Zhu, L., 2010. Shallow low-velocity zone of the San Jacinto fault from local earthquake waveform modelling, *Geophys. J. Int.,* **183,** 421–432.

Yang, H., Zhu, L. & Cochran, E.S., 2011. Seismic structures of the Calico fault zone inferred from local earthquake travel time modelling, *Geophys. J. Int.,* **186**, 760–770.

Zheng, G. & Rice, J.R., 1998. Conditions under which velocity-weakening friction allows a self-healing versus a crack-like mode of rupture, *Bull. seism. Soc. Am.,* **88,** 1466–1483.